arXiv:2610.23197v2 [cond-mat.mes-hall] 19 Oct 2026

Non-Adiabatic Spin-Induced Currents in Magnetic Weyl Semimetals

Kota Watanabe[1], Akihiro Ozawa[2,3], Hiroaki Ishizuka[4], Hiroki Isobe[1], Kentaro Nomura[1,5]

[1]*Department of Physics, Kyushu University, Fukuoka 819-0395, Japan*
[2]*Institut für Theoretische Physik, Universität Leipzig, 04103 Leipzig, Germany*
[3]*Institute for Solid State Physics, The University of Tokyo, Kashiwa 277-8581, Japan*
[4]*Department of Physics, Institute of Science Tokyo, Meguro, Tokyo 152-8551, Japan*
[5]*Quantum and Spacetime Research Institute, Kyushu University, Fukuoka 819-0395, Japan*

We theoretically study dc electric currents induced by rapid spin precession in noncentrosymmetric magnetic Weyl semimetals using the Floquet–Keldysh Green's-function formalism. The spin dynamics act as a time-dependent chiral gauge field and the geometric structure of electric currents is expressed in terms of the Berry curvature, the quantum metric, and the shift vector. For an isotropic Weyl cone, only an injection current is generated. This current scales quadratically with the driving frequency and linearly with the relaxation time associated with coupling to a fermionic bath. We further show that a finite Weyl-cone tilt modifies the available interband-transition phase space, smooths the frequency dependence of the current, and allows for a shift current and another type of injection current, both of which flow in directions determined by the tilt and the direction of the precession. A finite net current can remain after summing contributions from Weyl nodes of opposite chiralities when their transition phase spaces are inequivalent.

I. INTRODUCTION

Magnets hosting strong exchange interactions can exhibit nontrivial cross-correlated responses, such as the generation of an electric current driven by magnetization dynamics [1–3]. The emergence of such cross-correlated phenomena requires a low-symmetry environment, specifically the simultaneous breaking of spatial inversion ($\mathcal{P}$) and time-reversal ($\mathcal{T}$) symmetries [4, 5]. The investigation of these phenomena is driven by the aim of spintronics to develop faster, more efficient, and highly precise devices [6, 7]. Achieving this goal requires a comprehensive understanding of rapid magnetization dynamics and their non-equilibrium interplay with itinerant electrons [8, 9].

Therefore, we focus on magnetic Weyl semimetals (MWSMs) as an ideal platform for this pursuit, as they satisfy the necessary symmetry requirements while featuring strong interactions between topological conduction electrons and localized spins [10–16]. Noncentrosymmetric MWSMs considered here lacking inversion symmetry exhibit nonlinear responses driven by magnetization, promising a structure as rich as, if not richer than, conventional optical responses [5, 14, 17]. Despite this potential, existing studies on spin-induced electric currents have largely been confined to the adiabatic regime, where spin fluctuations are sufficiently slow [5, 18]. The cross-correlated electric current response in the non-adiabatic regime, where fast magnetization dynamics drive the system out of equilibrium, remains a crucial yet unexplored frontier.

In this paper, we investigate a MWSM with broken $\mathcal{P}$ symmetry driven out of equilibrium by spin dynamics to explore non-adiabatic geometric transport. Specifically, we derive a formula for the spin-induced nonlinear electric current using the Floquet–Keldysh Green's function method [19–24]. This paper is organized as follows. We first introduce a simple continuum model of a MWSM under time-periodic spin precession. We then derive analytical expressions for the spin-induced current using the Keldysh Green's function formalism and Floquet theory (Sec. II). In Sec. III, we show that the resulting current is decomposed into shift-current and injection-current contributions, which are characterized by band-topological or geometrical quantities, such as the Berry curvature, the quantum metric, and the shift vector. We find that tilting of the Weyl cone induces a finite current with a characteristic dependence on the driving frequency. Then in Sec. IV, we evaluate the strength of the induced current based on the effective model of a certain MWSM, compensated ferrimagnetic Heusler system Ti_2MnAl.

II. METHOD

A. Model

We consider the following model of noncentrosymmetric magnetic Weyl semimetals (MWSMs) coupled to a ferromagnetic moment, whose effective Hamiltonian is given by [12, 25]

$$\mathcal{H}_{\mathrm{MWSM}}(t) = \begin{pmatrix} -iv\boldsymbol{\sigma}\cdot\boldsymbol{\nabla} - J_{\mathrm{exc}}\boldsymbol{m}(t)\cdot\boldsymbol{\sigma} - (\mu+\Delta/2)\sigma_0 & 0 \\ 0 & iv\boldsymbol{\sigma}\cdot\boldsymbol{\nabla} - J_{\mathrm{exc}}\boldsymbol{m}(t)\cdot\boldsymbol{\sigma} - (\mu-\Delta/2)\sigma_0 \end{pmatrix}, \tag{1}$$

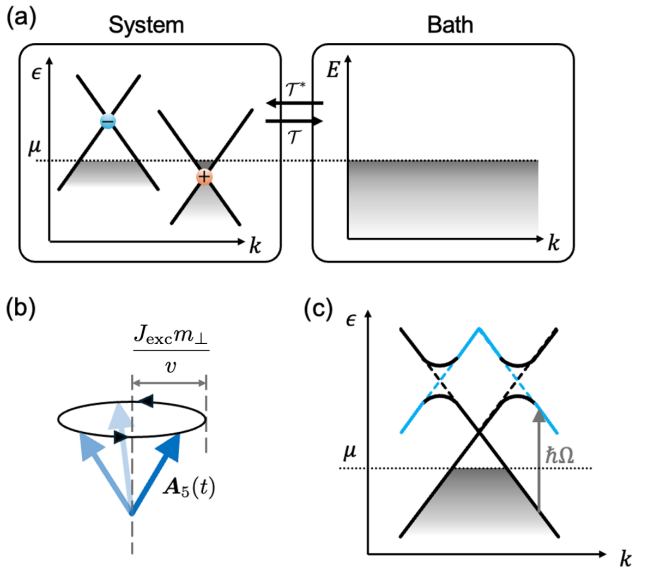


FIG. 1. Model of the driven MWSM. (a) Band structure of a MWSM lacking inversion ($\mathcal{P}$) symmetry, indicating the distinct chemical potentials of opposite chirality. The tunneling coefficient between the system and the bath is denoted by $\mathcal{T}$. $\mathcal{T}^*$ for the process from the bath to the system. (b) The effective chiral gauge field A_5 induced as a perturbation.(c) The relevant Floquet band sector, highlighting the resonance between the one-photon-dressed valence band and the bare conduction band.

where v is the Fermi velocity, $J_{\rm exc}$ is the exchange coupling constant, and Δ denotes the energy splitting between the two Weyl nodes (see Fig. 1-(a), 2). To be specific, we consider a magnetic precession about the z axis, in which case $\boldsymbol{m}(t)$ reads

$$\boldsymbol{m}(t) = \delta\boldsymbol{m}(t) + \boldsymbol{m}_0, \tag{2}$$

$$\delta\boldsymbol{m}(t) = m_\perp(\cos\Omega t, \sin\Omega t, 0)^T, \tag{3}$$

$$\boldsymbol{m}_0 = \left(0, 0, \sqrt{1-m_\perp^2}\right)^T. \tag{4}$$

By absorbing the static magnetization into the momentum as $\boldsymbol{k} \equiv -i\boldsymbol{\nabla} - sJ_{\rm exc}\boldsymbol{m}_0/v$, and introducing the chiral gauge field $\boldsymbol{A}_5(t) \equiv J_{\rm exc}\delta\boldsymbol{m}(t)/v$ [26, 27], we can compactly rewrite the single node Hamiltonian as

$$\mathcal{H}(t) = sv(\boldsymbol{k} - s\boldsymbol{A}_5(t))\cdot\boldsymbol{\sigma} - \left(\mu + s\frac{\Delta}{2}\right)\sigma_0, \tag{5}$$

where $s = \pm 1$ labels the chirality of the Weyl node (see 1-(b)).

To treat the chirality and band indices in a unified and compact manner, we parameterize the momentum vector as $\boldsymbol{k} = k(\sin\theta\cos\phi, \sin\theta\sin\phi, \cos\theta)^T$ with $k \equiv |\boldsymbol{k}|$, and define the standard eigenstates of the chirality operator $\boldsymbol{k}\cdot\boldsymbol{\sigma}$ as follows:

$$(\boldsymbol{k}\cdot\boldsymbol{\sigma})\,|\chi_\pm\rangle = \pm k\,|\chi_\pm\rangle\,,$$
$$|\chi_+\rangle = \begin{pmatrix}\cos\frac{\theta}{2}\\ e^{i\phi}\sin\frac{\theta}{2}\end{pmatrix}, \quad |\chi_-\rangle = \begin{pmatrix}\sin\frac{\theta}{2}\\ -e^{i\phi}\cos\frac{\theta}{2}\end{pmatrix}. \tag{6}$$

Using these basis states, the eigenvalue equation for the unperturbed Hamiltonian $\mathcal{H}_0 = sv\boldsymbol{k}\cdot\boldsymbol{\sigma} - (\mu + s\Delta/2)\sigma_0$ can be expressed for both chiralities $s = \pm 1$ as

$$\mathcal{H}_0\,|u_n^s\rangle = \epsilon_n^s\,|u_n^s\rangle\,, \quad (n = 1, 2) \tag{7}$$

where the band energies and their corresponding eigenspinors are explicitly given by

$$\epsilon_2^s = vk - \left(\mu + s\frac{\Delta}{2}\right), \quad |u_2^s\rangle = |\chi_{+s}\rangle\,, \tag{8}$$

$$\epsilon_1^s = -vk - \left(\mu + s\frac{\Delta}{2}\right), \quad |u_1^s\rangle = |\chi_{-s}\rangle\,, \tag{9}$$

with the indices 2 and 1 denoting the conduction and valence bands, respectively. Using this notation, we define the matrix elements of a generic Hermitian operator $\mathcal{O}$ as

$$\mathcal{O}_{ij} \equiv \langle u_i^s|\,\mathcal{O}\,|u_j^s\rangle\,, \tag{10}$$

where i and j denote the band indices.

We model dissipation by coupling the system to an equilibrium fermionic reservoir with chemical potential μ and inverse temperature $\beta > 0$ (Fig. 1(a)). Within the wide-band approximation, the reservoir hybridization is assumed to be energy independent over the relevant energy window; after absorbing the constant real part into the system Hamiltonian, the retarded self-energy reduces to a frequency-independent imaginary broadening characterized by Γ (see Appendix A). This featureless bath provides a phenomenological description of relaxation by encoding the net effect of the environment into a single parameter, and therefore Γ should not be identified with the rate of any specific microscopic scattering mechanism [23, 28, 29].

B. Floquet effective Hamiltonian

Since the magnetization $\boldsymbol{m}(t)$ precesses with frequency Ω, i.e. the Hamiltonian $\mathcal{H}(t)$ has the time periodicity of $T \equiv 2\pi/\Omega$, we expand the Hamiltonian into its Fourier components:

$$H_n(\boldsymbol{k}) = \int_0^T \frac{dt}{T} e^{in\Omega t}\mathcal{H}(\boldsymbol{k}, t). \tag{11}$$

Decomposing $\boldsymbol{A}_5(t) = \boldsymbol{A}_{5,\Omega}e^{-i\Omega t} + \boldsymbol{A}_{5,\Omega}^* e^{i\Omega t}$, yielding

$$\boldsymbol{A}_{5,\Omega} = \frac{J_{\rm exc}m_\perp}{2v}(1, i, 0)^T = \frac{A_5}{\sqrt{2}}(1, i, 0)^T, \tag{12}$$

where $A_5 \equiv J_{\rm exc}m_\perp/(\sqrt{2}v)$, the unperturbed Hamiltonian H_0 and the coupling component H_1 are given

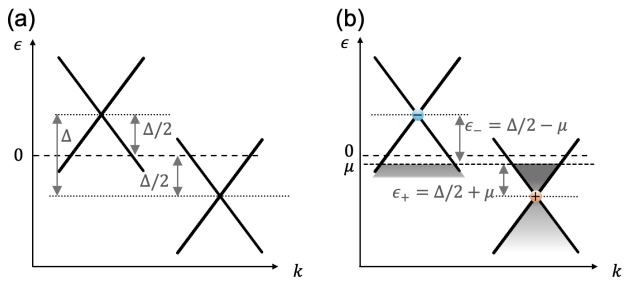


FIG. 2. Schematic illustration of the energy offset between Weyl nodes. (a) The energy splitting between the two Weyl nodes is denoted by Δ, with the nodes symmetrically displaced by $\pm\Delta/2$ relative to the reference energy $\epsilon = 0$. (b) Assuming the $s = -1$ Weyl node is located at a higher energy than the $s = +1$ Weyl node, the energy differences relative to the chemical potential μ are given by $\epsilon_- = \Delta/2 - \mu$ for the $s = -1$ node and $\epsilon_+ = -(\Delta/2+\mu)$ for the $s = +1$ Weyl node. The gray areas indicate the occupied electronic states.

by $H_0 = sv\boldsymbol{k}\cdot\boldsymbol{\sigma} - (\mu + s\Delta/2)\sigma_0 = \mathcal{H}_0$ and $H_1 = -v\boldsymbol{A}_{5,\Omega}\cdot\boldsymbol{\sigma}$, $H_{-1} = -v\boldsymbol{A}^*_{5,\Omega}\cdot\boldsymbol{\sigma}$. Using the Floquet formalism detailed in Appendix A, the effective Hamiltonian of the system is given by [30, 31]

$$(H_F)_{l,n} \equiv H_{l-n} - n\Omega\delta_{l,n}. \tag{13}$$

To explicitly calculate the electric current, we reduce the infinite-dimensional Floquet space to a tractable subspace [23]. Focusing on the single-photon processes, we truncate the Floquet space to the resonant subspace spanned by $n = 0$ and -1 (see Fig. 1(c)). The Floquet effective Hamiltonian in this truncated subspace is given by [32]

$$\begin{aligned} H_F^{2\times2} &= \begin{pmatrix} \epsilon_1 + \Omega & -s\frac{A_5}{\sqrt{2}}(v^x_{12} - iv^y_{12}) \\ -s\frac{A_5}{\sqrt{2}}(v^x_{21} + iv^y_{21}) & \epsilon_2 \end{pmatrix} \\ &= h_0\tau_0 + \boldsymbol{h}\cdot\boldsymbol{\tau}, \end{aligned} \tag{14}$$

where the velocity matrix elements v^a_{ij} are defined as $v^a_{ij} \equiv \langle u^s_i|\,\partial_a\mathcal{H}_0\,|u^s_j\rangle$ (see 1-(c)).

The Floquet formalism requires the time periodicity of the Hamiltonian, $\mathcal{H}(t+T) = \mathcal{H}(t)$, and therefore remains applicable to the gapless Weyl spectrum [30, 31]. In the present system, the relevant non-adiabatic response arises from the one-photon resonance, $\epsilon_2 - \epsilon_1 \approx \hbar\Omega$. Since $\epsilon_2 - \epsilon_1 = 2vk$, the resonant surface is determined by $2vk = \hbar\Omega$. The interband transitions are further restricted by Pauli blocking, $\hbar\Omega \gtrsim 2|\mu + s\Delta/2|$. Thus, Δ is not a band gap required for the Floquet formalism, but it sets the characteristic energy scale of the resonant response, $\hbar\Omega \sim \Delta$, up to the chemical-potential shift (see Fig. 1-(a)).

Near the one-photon resonance, the one-photon-dressed valence band $|u_1, -1\rangle$ and the bare conduction band $|u_2, 0\rangle$ become nearly degenerate, $\epsilon_1 + \hbar\Omega \approx \epsilon_2$. The dominant resonant subspace is therefore described by the 2×2 Floquet effective Hamiltonian (14). The reduction to this two-level subspace is justified within the rotating-wave approximation when the coupling between Floquet sectors is sufficiently smaller than their energy separation, $|A_{5,\Omega}\cdot\boldsymbol{v}_{12}|, \Gamma \ll \hbar\Omega$. Under this condition, the off-resonant Floquet sectors give only higher-order corrections and can be neglected [24, 32]. Thus, the periodicity guarantees the Floquet description, whereas the near-resonance condition and weak intersector coupling justify the effective 2×2 reduction.

Its coefficients in the Pauli matrix representation by using τ, which is two-level Floquet basis, are given by

$$h_0 = \frac{(\epsilon_1 + \Omega) + \epsilon_2}{2}, \quad h_z = \frac{(\epsilon_1 + \Omega) - \epsilon_2}{2}, \tag{15}$$

$$h_x + ih_y = -s\frac{A_5}{\sqrt{2}}\,(v^x_{21} + iv^y_{21})\,, \tag{16}$$

$$h_x - ih_y = -s\frac{A_5}{\sqrt{2}}\,(v^x_{12} - iv^y_{12})\,. \tag{17}$$

Focusing on the two Floquet bands that cross, we construct an effective Hamiltonian and decompose the group velocity into identity and Pauli matrix components:

$$\begin{aligned} &\tilde{v}^a \equiv \\ &\begin{pmatrix} \partial_a\epsilon_1 & -s\frac{A_5}{\sqrt{2}}((\partial_a v^x)_{12} - i(\partial_a v^y)_{12}) \\ -s\frac{A_5}{\sqrt{2}}((\partial_a v^x)_{21} + i(\partial_a v^y)_{21}) & \partial_a\epsilon_2 \end{pmatrix} \\ &= \tilde{v}^a_0\tau_0 + \tilde{\boldsymbol{v}}^a\cdot\boldsymbol{\tau}, \end{aligned} \tag{18}$$

with the coefficients given by

$$\tilde{v}^a_0 = \frac{v^a_{11} + v^a_{22}}{2}, \quad \tilde{v}^a_z = \frac{v^a_{11} - v^a_{22}}{2}, \tag{19}$$

$$\tilde{v}^a_x + i\tilde{v}^a_y = -s\frac{A_5}{\sqrt{2}}\,[(\partial_a v^x)_{21} + i(\partial_a v^y)_{21}]\,, \tag{20}$$

$$\tilde{v}^a_x - i\tilde{v}^a_y = -s\frac{A_5}{\sqrt{2}}\,[(\partial_a v^x)_{12} - i(\partial_a v^y)_{12}]\,, \tag{21}$$

and we use the notation $\partial_a \equiv \partial/\partial k_a$. Within this two-level Floquet basis $\boldsymbol{\tau}$, the lesser component of the self-energy in frequency space takes a diagonal form because of the wide-band approximation:

$$\boldsymbol{\Sigma}^<(\omega) = i\Gamma\begin{pmatrix} f(\omega - \Omega) & 0 \\ 0 & f(\omega) \end{pmatrix}, \tag{22}$$

where $\tau = 1/(2\Gamma)$ represents the relaxation time, and $f(\omega)$ denotes the Fermi distribution function of the bath. The bold indicates the matrix of the 2×2 Floquet basis.

To evaluate the lesser Green's function via the Dyson equation,

$$\boldsymbol{G}^<(\omega) = \boldsymbol{G}^R(\omega)\boldsymbol{\Sigma}^<(\omega)\boldsymbol{G}^A(\omega), \tag{23}$$

we first require the retarded and advanced Green's functions (see Appendix A). Within the truncated two-level Floquet subspace, these can be explicitly determined

from the reduced Floquet effective Hamiltonian $H_F^{2\times2}$ as follows:

$$\boldsymbol{G}^{R/A}(\omega) = \frac{(\omega - h_0 \pm i\Gamma/2)\sigma_0 + \boldsymbol{h}\cdot\boldsymbol{\tau}}{(\omega - h_0 \pm i\Gamma/2)^2 - h^2}, \tag{24}$$

where $h \equiv |\boldsymbol{h}|$, $\boldsymbol{h} \equiv (h_x, h_y, h_z)^T$.

III. RESULTS

The a-component of the electric current density induced by the magnetization precession in the xy plane is determined by the lesser Green's function as

$$\bar{J}^{a;xy} \equiv -i\int \frac{d\boldsymbol{k}}{(2\pi)^3}\int \frac{d\omega}{2\pi}\,\mathrm{Tr}\left[\tilde{v}^a(\boldsymbol{k})\boldsymbol{G}^<(\boldsymbol{k},\omega)\right], \tag{25}$$

where $d\boldsymbol{k} \equiv dk_x dk_y dk_z$.

Performing the frequency integration and extracting the time-independent component, the total DC electric current can be decomposed into two contributions. Eq. (25) reduces to

$$\bar{J}^{a;xy} = \bar{J}^{a;xy}_{\mathrm{shift}} + \bar{J}^{a;xy}_{\mathrm{inj}}, \tag{26}$$

where

$$\bar{J}^{a;xy}_{\mathrm{shift}} \equiv \int \frac{d\boldsymbol{k}}{(2\pi)^3}\frac{\Gamma}{4}\frac{[\tilde{\boldsymbol{v}}^a\times\boldsymbol{h}]_z}{h^2+\Gamma^2/4}\delta f, \tag{27}$$

$$\bar{J}^{a;xy}_{\mathrm{inj}} \equiv \int \frac{d\boldsymbol{k}}{(2\pi)^3}\frac{1}{2}\frac{h_z(\tilde{\boldsymbol{v}}^a\cdot\boldsymbol{h}) + \tilde{v}^a_z\Gamma^2/4}{h^2+\Gamma^2/4}\delta f. \tag{28}$$

Here, we have introduced the combination of Fermi distribution functions $\delta f \equiv f(h_0+h-\Omega)+f(h_0-h-\Omega)-f(h_0+h)-f(h_0-h)$, following Ref. [23], and defined $\boldsymbol{h} \equiv (h_x,h_y,h_z)^T$, $\tilde{\boldsymbol{v}}^a \equiv (\tilde{v}^a_x,\tilde{v}^a_y,\tilde{v}^a_z)^T$. We classify these two contributions according to their dependence on the relaxation rate Γ and refer to them as the shift and injection currents, respectively. The physical origin of this correspondence will be clarified below.

A. Perturbative Limit

We now consider the perturbative regime $|\boldsymbol{A}_{5,\Omega}\cdot\boldsymbol{v}_{12}| \ll \Gamma$, where the off-diagonal hybridization amplitude of the Floquet effective Hamiltonian is much smaller than the relaxation rate Γ induced by the coupling to the bath. When the resonance width is also sufficiently small compared with the characteristic energy scale of the interband transition, the Lorentzian factor associated with spectral broadening becomes sharply peaked near resonance. It can then be approximated by a Dirac delta function as

$$\frac{1}{h^2+\Gamma^2/4} \approx \frac{4\pi}{\Gamma}\delta(\epsilon_{12}+\Omega). \tag{29}$$

Here, the delta-function form should be understood as a narrow-resonance approximation. More generally, retaining the drive-induced hybridization $\sqrt{h_x^2+h_y^2}$ gives [24]

$$\frac{1}{h_z^2+h_x^2+h_y^2+\Gamma^2/4} \approx \frac{\pi}{\sqrt{h_x^2+h_y^2+\Gamma^2/4}}\delta(h_z). \tag{30}$$

In the perturbative regime $\sqrt{h_x^2+h_y^2} \ll \Gamma$, this expression reduces to Eq. (29), with corrections of order $O[(h_x^2+h_y^2)/\Gamma^2]$. For the Weyl model considered here, the present resonance-shell approximation is therefore justified under the hierarchy $\sqrt{h_x^2+h_y^2} \ll \Gamma \ll \Omega$. Note that for $\sqrt{h_x^2+h_y^2} \gtrsim \Gamma$, nonperturbative Rabi saturation becomes important and modifies both the magnitude and the relaxation-time dependence of the current [24].

Using Eq. (29), the resonance condition selects the interband transitions satisfying

$$\epsilon_2 - \Omega = \epsilon_1. \tag{31}$$

Consequently, the combination of Fermi distribution functions reduces to

$$\begin{aligned}\delta f &= f(\epsilon_1)+f(\epsilon_2-\Omega)-f(\epsilon_1+\Omega)-f(\epsilon_2)\\ &= f(\epsilon_1)+f(\epsilon_1)-f(\epsilon_2)-f(\epsilon_2)\\ &= 2\Big(f(\epsilon_1)-f(\epsilon_2)\Big) \equiv 2f_{12}.\end{aligned} \tag{32}$$

B. Geometric Representation of Nonlinear Electric Current

For a better understanding of Eqs. (27)–(28), we look into their connection to the geometric properties of electronic states. To this end, here we review geometric quantities that characterizes the electron bands. One such quantity is the Berry connection defined as $\mathcal{A}^a_{ij} \equiv -i\langle u^s_i|\partial_a u^s_j\rangle$, where i, j denote the band indices. For the interband transitions ($i \neq j$), the quantum metric and the interband Berry curvature are given by the product of the Berry connections [33, 34]:

$$\mathcal{G}^{ab}_{ij} \equiv \mathrm{Re}[\mathcal{A}^a_{ij}\mathcal{A}^b_{ji}], \quad \mathcal{F}^{ab}_{ij} \equiv 2\mathrm{Im}[\mathcal{A}^a_{ij}\mathcal{A}^b_{ji}]. \tag{33}$$

Using the DC electric current formulas given in Eqs. (27)–(28), we obtain the explicit expressions

$$\begin{aligned}\bar{J}^{a;xy}_{\mathrm{shift},s} =& \pi(\Omega A_5)^2\int\frac{d\boldsymbol{k}}{(2\pi)^3}R^{a;xy}_{12,-}\\ &\times(\mathcal{G}^{xx}_{12}+\mathcal{G}^{yy}_{12}-\mathcal{F}^{xy}_{12})\,f_{12}\delta(\epsilon_1-\epsilon_2+\Omega),\end{aligned} \tag{34}$$

$$\begin{aligned}\bar{J}^{a:xy}_{\mathrm{inj},L,s} =& -2\pi\tau(\Omega A_5)^2\int\frac{d\boldsymbol{k}}{(2\pi)^3}(v^a_{11}-v^a_{22})\\ &\times(\mathcal{G}^{xx}_{12}+\mathcal{G}^{yy}_{12})\,f_{12}\delta(\epsilon_1-\epsilon_2+\Omega),\end{aligned} \tag{35}$$

$$\begin{aligned}\bar{J}^{a;xy}_{\mathrm{inj},C,s} =& 2\pi\tau(\Omega A_5)^2\int\frac{d\boldsymbol{k}}{(2\pi)^3}(v^a_{11}-v^a_{22})\\ &\times\mathcal{F}^{xy}_{12}\,f_{12}\delta(\epsilon_1-\epsilon_2+\Omega).\end{aligned} \tag{36}$$

Here, the total injection and shift currents are defined as $\bar{J}^{a;xy}_{\rm inj} \equiv \bar{J}^{a;xy}_{\rm inj,L} + \bar{J}^{a;xy}_{\rm inj,C}$, $\bar{J}^{a;xy}_{\rm shift} \equiv \bar{J}^{a;xy}_{\rm shift,L} + \bar{J}^{a;xy}_{\rm shift,C}$, respectively, and $R^{a;bc}_{12,\pm} \equiv \partial_a \arg\left(v^b_{12} \pm i v^c_{12}\right) + \mathcal{A}^a_{11} - \mathcal{A}^a_{22}$ is the shift vector. The subscripts L and C denote the linear and circular components, respectively, associated with the symmetric and antisymmetric parts of the charge-current response kernel. Detailed derivations of these expressions are provided in Appendix B.

For the Hamiltonian in Eq. (34)-(36), the currents read

$$\bar{J}^{z;xy}_{{\rm shift},s} = 0, \tag{37}$$

$$\bar{J}^{z;xy}_{{\rm inj},s} = \bar{J}^{z;xy}_{{\rm inj},C,s} = s\tau \frac{\Omega^2 A_5^2}{6\pi} \Theta\left(\Omega - 2\left|\mu + s\frac{\Delta}{2}\right|\right), \tag{38}$$

in deriving which we used

$$\begin{aligned} f_{12} &= \Theta\left(\Omega + 2\left(\mu + s\frac{\Delta}{2}\right)\right) - \Theta\left(\Omega - 2\left(\mu - s\frac{\Delta}{2}\right)\right) \\ &= \Theta\left(\Omega - 2\left|\mu + s\frac{\Delta}{2}\right|\right). \end{aligned} \tag{39}$$

Here, we apply the absolute zero limit $f(\epsilon) \to \Theta(-\epsilon)$. Consequently, the total DC current generated from a single Weyl node is given by

$$\begin{aligned} \bar{J}^{z;xy}_{s} &\equiv \bar{J}^{z;xy}_{{\rm shift},s} + \bar{J}^{z;xy}_{{\rm inj},s} \\ &= s\tau \frac{\Omega^2 A_5^2}{6\pi} \Theta\left(\Omega - 2\left|\mu + s\frac{\Delta}{2}\right|\right). \end{aligned} \tag{40}$$

In a system without inversion symmetry where the chemical potentials of the two Weyl nodes differ, assuming that the $s = -1$ node has higher energy than $s = +1$ (see Fig. 2), the total macroscopic current $\bar{J}^z_{\rm total} \equiv \bar{J}^z_- + \bar{J}^z_+$ exhibits piecewise behavior depending on the driving frequency Ω:

$$\bar{J}^z_{\rm total} = \frac{\tau \Omega^2 A_5^2}{6\pi} \sum_{s=\pm 1} s\,\Theta\left(\Omega - 2\left|\mu + s\frac{\Delta}{2}\right|\right) \tag{41}$$

$$= \begin{cases} 0 & (\Omega < \Delta + 2\mu) \\ \bar{J}^z_+ & (\Delta + 2\mu < \Omega < \Delta - 2\mu) \\ 0 & (\Omega > \Delta - 2\mu) \end{cases}, \tag{42}$$

If we assume the opposite configuration of the Weyl nodes, the "+" and "−" signs in (42) are reversed.

C. DC Current in a Tilted Weyl Semimetal

In what follows, we analytically evaluate the spin-induced DC current in the tilted case. We will demonstrate that the current response exhibits discontinuous "jumps" in untilted Weyl semimetals, and further reveal that these abrupt jumps are significantly smoothed out when the Weyl cone is tilted. For simplicity in the subsequent analysis, we assume that the "−" node resides at a higher energy than the "+" node.

Compared to the original model, the Hamiltonian of the tilted Weyl semimetal includes an additional tilt term along the z-axis [35]:

$$\mathcal{H}'_0 = \mathcal{H}_0 - suk_z\sigma_0, \tag{43}$$

where the tilt parameter u is assumed to satisfy $u/v < 1$, which is the condition for a type-I Weyl semimetal. This modification shifts only the energy eigenvalues without altering the eigenstates:

$$\epsilon'_1 = \epsilon_1 - suk_z, \quad \epsilon'_2 = \epsilon_2 - suk_z. \tag{44}$$

Consequently, the effect of the tilt enters the current integrals purely through the modified Fermi distribution function:

$$f_{12} \to f(\epsilon_1 - suk_z) - f(\epsilon_2 - suk_z). \tag{45}$$

We can explicitly determine the integration bounds governed by Fermi surface constraints. By the discussion, the DC electric current components are analytically evaluated as

$$\bar{J}^{z;xy}_{{\rm inj},L,s} = \tau \frac{\Omega^2 A_5^2}{8\pi} \int_{-\bar{k}}^{\bar{k}} \frac{dk_z}{\bar{k}} \frac{k_z}{\bar{k}} \left(1 + \frac{k_z^2}{\bar{k}^2}\right) f_{12}, \tag{46}$$

$$\bar{J}^{z;xy}_{{\rm inj},C,s} = s\tau \frac{\Omega^2 A_5^2}{4\pi} \int_{-\bar{k}}^{\bar{k}} \frac{dk_z}{\bar{k}} \left(\frac{k_z}{\bar{k}}\right)^2 f_{12}. \tag{47}$$

Here, we apply the absolute zero limit $f(\epsilon) \to \Theta(-\epsilon)$ and we apply the following formulas to the theta function in the DC electric current:

$$\begin{aligned} f_{12}|_{s=+1} =& \Theta\left[\mu + s\frac{\Delta}{2} + v\bar{k} + suk_z\right] \\ & - \Theta\left[\mu + s\frac{\Delta}{2} - v\bar{k} + suk_z\right]. \end{aligned} \tag{48}$$

where the resonance condition $v\bar{k} = \Omega/2$ has been used.

On the resonant surface $k = \bar{k}$, the relevant threshold momenta are determined by the Fermi-level crossings of the conduction band at the $s = +1$ node and the valence band at the $s = -1$ node:

$$\begin{aligned} \epsilon'^{+}_2(K_+) &= v\bar{k} - \left(\mu + \frac{\Delta}{2}\right) - uK_+ = 0, \\ \epsilon'^{-}_1(K_-) &= -v\bar{k} - \left(\mu - \frac{\Delta}{2}\right) + uK_- = 0. \end{aligned} \tag{49}$$

Using $v\bar{k} = \Omega/2$, the two threshold momenta are compactly written as

$$K_\pm = \frac{v\bar{k}}{u}\left(1 - \frac{\Delta \pm 2\mu}{2v\bar{k}}\right). \tag{50}$$

After combining the contributions from the two Weyl nodes, the Pauli-blocking constraints can be expressed in terms of K_+ and K_-. Taking into account the physical range $-\bar{k} \le k_z \le \bar{k}$, the relevant integration interval is determined by the intersection of these threshold momenta with the resonant momentum sphere.

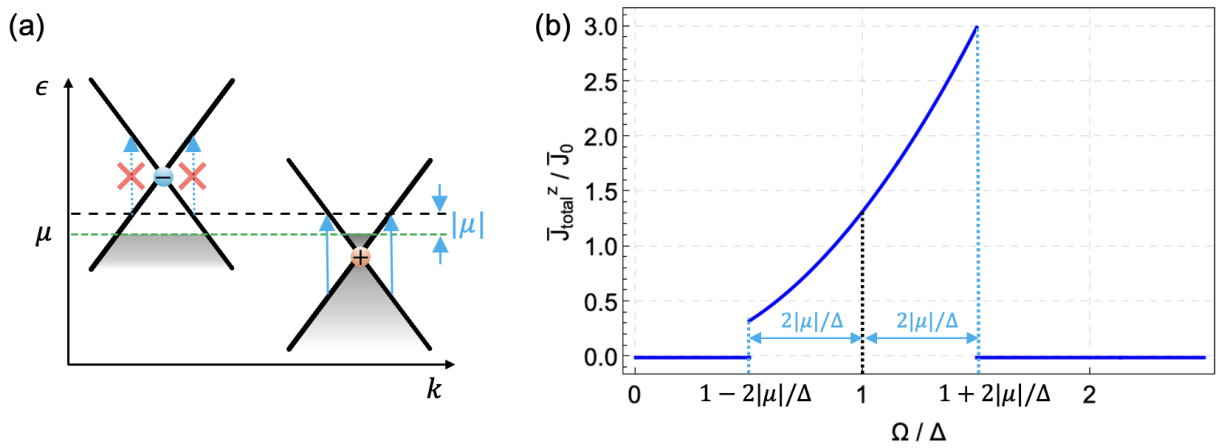


FIG. 3. Frequency dependence of the current induced by spin precession for the potential $-\Delta/2 \le \mu \le 0$. (a) Schematic of the interband transitions induced by spin precession at two Weyl nodes separated in energy by Δ. The gray regions represent occupied states, and the chemical potential lies a distance $|\mu|$ from the lower-energy $s = +1$ Weyl node. The blue arrows indicate drive-induced transitions. The transition at the $s = +1$ node is allowed, whereas that at the $s = -1$ node is forbidden by the emptiness of the initial state, as indicated by the red crosses. (b) Frequency dependence of the normalized total DC current $\bar{J}_{\rm total}/\bar{J}_0$ generated by spin precession, where $\bar{J}_0 = \Delta A_5^2/(2\pi)$ and $\tau = 1.0$. The spin-precession frequency Ω is normalized by the energy separation Δ between the Weyl nodes. For $\Omega/\Delta < 1-2|\mu|/\Delta$, the transition at one Weyl node is energetically forbidden, while that at the other node is Pauli blocked; consequently, the total current vanishes. In the intermediate-frequency window $1 - 2|\mu|/\Delta < \Omega/\Delta < 1 + 2|\mu|/\Delta$, only one Weyl node contributes, resulting in a finite net current. For $\Omega/\Delta > 1 + 2|\mu|/\Delta$, spin-precession-induced transitions are allowed at both Weyl nodes, and their oppositely directed current contributions cancel.

Considering the regime in which the $s = -1$ Weyl node is located at $\Delta/2 - \mu > 0$, while the $s = +1$ Weyl node is located at $-\Delta/2 - \mu < 0$, we obtain

$$
\begin{aligned}
&f_{12}|_{s=+1} - f_{12}|_{s=-1} \\
&= 1 - \Theta\Big[k_z - \frac{v}{u}\bar{k}\Big(1 - \frac{\Delta + 2\mu}{2v\bar{k}}\Big)\Big] \\
&\quad - \Big\{\Theta\Big[\frac{v}{u}\bar{k}\Big(1 - \frac{\Delta - 2\mu}{2v\bar{k}}\Big) - k_z\Big] - 0\Big\} \\
&= \Theta(K_+ - k_z) - \Theta(K_- - k_z), \qquad (51) \\
&f_{12}|_{s=+1} + f_{12}|_{s=-1} \\
&= 1 - \Theta\Big[k_z - \frac{v}{u}\bar{k}\Big(1 - \frac{\Delta + 2\mu}{2v\bar{k}}\Big)\Big] \\
&\quad + \Theta\Big[\frac{v}{u}\bar{k}\Big(1 - \frac{\Delta - 2\mu}{2v\bar{k}}\Big) - k_z\Big] - 0 \\
&= \Theta(K_+ - k_z) + \Theta(K_- - k_z) \\
&= 2\Theta(K_+ - k_z) - \Big(\Theta(K_+ - k_z) - \Theta(K_- - k_z)\Big). \qquad (52)
\end{aligned}
$$

Consequently,

$$
\begin{aligned}
&\bar{J}^{z;xy}_{{\rm inj},C,+} + \bar{J}^{z;xy}_{{\rm inj},C,-} \\
&= \tau\frac{\Omega^2 A_5^2}{4\pi}\int_{\max\{-\bar{k},K_-\}}^{\min\{\bar{k},K_+\}} \frac{dk_z}{\bar{k}}\Big(\frac{k_z}{\bar{k}}\Big)^2, \\
&\bar{J}^{z;xy}_{{\rm inj},L,+} + \bar{J}^{z;xy}_{{\rm inj},L,-} \\
&= 2\tau\frac{\Omega^2 A_5^2}{8\pi}\int_{-\bar{k}}^{\min\{\bar{k},K_+\}} \frac{dk_z}{\bar{k}}\frac{k_z}{\bar{k}}\Big(1 + \frac{k_z^2}{k^2}\Big) \\
&\quad - \tau\frac{\Omega^2 A_5^2}{8\pi}\int_{\max\{-\bar{k},K_-\}}^{\min\{\bar{k},K_+\}} \frac{dk_z}{\bar{k}}\frac{k_z}{\bar{k}}\Big(1 + \frac{k_z^2}{k^2}\Big). \qquad (53)
\end{aligned}
$$

By comparing the integration bounds under the type-I condition $u/v < 1$, the explicit form of the integral can be determined for each parameter regime. In the untilted limit, $u \to 0$, the Fermi-surface constraint reduces to that of the untilted Weyl semimetal, reproducing the results obtained in the previous section. The integration range $k_z \in [\max\{-\bar{k}, K_-\}, \min\{\bar{k}, K_+\}]$ is determined by the intersection between the Pauli-allowed region and the resonant momentum surface (see Fig. 4) [36].

By comparing the integration bounds under the type-I condition $0 < u/v < 1$, the integral can be evaluated explicitly in each parameter regime. In the untilted limit, $u \to 0$, the constraints imposed by the occupation factors reduce to those of an untilted Weyl semimetal, and the results obtained in the previous section are recovered.

The integration interval $k_z \in [\max\{-\bar{k}, K_-\}, \min\{\bar{k}, K_+\}]$ is determined by the overlap between the constant-energy shell selected by the resonance condition and the region in which the interband transitions are not Pauli blocked (see Fig. 4) [36]. For the isotropic Weyl dispersion considered here, the resonance condition fixes the momentum magnitude to $\bar{k} = \Omega/(2v)$.

For $\mu/\Delta \le 0$ and $\Omega/\Delta > 1$, the integration bounds

TABLE I. Nonvanishing current components and their azimuthally integrated geometric kernels for an isotropic Weyl cone with a tilt along the z direction. The expressions are shown for $\eta = +1$ and the reference chirality $s = +1$. All current-axis components not listed in the table vanish upon integration over the azimuthal angle ϕ.

Precession	Response	Nonzero current component
xy	Linear injection	$\bar{J}^{z;xy}_{\mathrm{inj,L}}$
xy	Circular injection	$\bar{J}^{z;xy}_{\mathrm{inj,C}}$
yz	Linear injection	$\bar{J}^{z;yz}_{\mathrm{inj,L}}$
yz	Circular injection	$\bar{J}^{x;yz}_{\mathrm{inj,C}}$
yz	Shift	$\bar{J}^{y;yz}_{\mathrm{shift}}$
zx	Linear injection	$\bar{J}^{z;zx}_{\mathrm{inj,L}}$
zx	Circular injection	$\bar{J}^{y;zx}_{\mathrm{inj,C}}$
zx	Shift	$\bar{J}^{x;zx}_{\mathrm{shift}}$

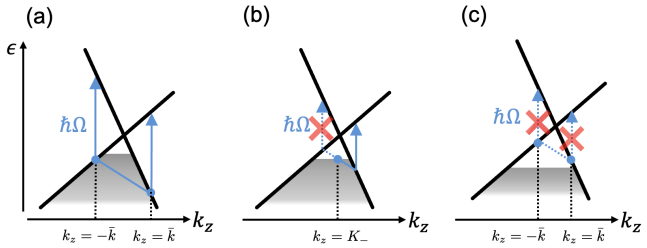


FIG. 4. Schematic illustrating the different cases for the lower integration bound. (a) When the resonant surface lies entirely below the chemical potential, the integration range begins at $-\bar{k} = \max\{-\bar{k}, K_-\}$. (b) When the chemical potential intersects the resonant surface, only the portion below the chemical potential contributes, restricting the lower integration bound to $K_- = \max\{-\bar{k}, K_-\}$. (c) When $K_- > \bar{k}$, the integration range completely collapses.

can be classified as follows:

$$\text{Case I}: \quad 1 < \frac{\Omega}{\Delta} < \frac{1-2\mu/\Delta}{1+u/v}, \quad \frac{u}{v} < -\frac{2\mu}{\Delta}, \tag{54}$$

$$\text{Case II}: \quad \frac{\Omega}{\Delta} > \max\left\{1, \frac{1-2\mu/\Delta}{1+u/v}, \frac{1+2\mu/\Delta}{1-u/v}\right\}, \tag{55}$$

$$\text{Case III}: \quad 1 < \frac{\Omega}{\Delta} < \frac{1+2\mu/\Delta}{1-u/v}, \quad \frac{u}{v} > -\frac{2\mu}{\Delta}. \tag{56}$$

Case I therefore occurs only when $u/v < -2\mu/\Delta$, whereas Case III occurs only when $u/v > -2\mu/\Delta$. At $u/v = -2\mu/\Delta$, the two frequency thresholds coincide with $\Omega/\Delta = 1$, and only Case II is realized within the assumed frequency range.

For the integration interval to have a finite width, the two conditions

$$K_- < \bar{k}, \quad K_+ > -\bar{k} \tag{57}$$

must be satisfied. Solving these inequalities for Ω/Δ gives

$$\frac{\Omega}{\Delta} < \frac{1-2\mu/\Delta}{1-u/v}, \quad \frac{\Omega}{\Delta} > \frac{1+2\mu/\Delta}{1+u/v}, \tag{58}$$

respectively. For $\mu/\Delta \leq 0$ and $0 < u/v < 1$, the second threshold is smaller than unity and is therefore automatically satisfied under the assumption $\Omega/\Delta > 1$. Consequently, the condition for a nonvanishing integration interval reduces to

$$1 < \frac{\Omega}{\Delta} < \frac{1-2\mu/\Delta}{1-u/v}. \tag{59}$$

In the untilted limit, this frequency window becomes $1 < \Omega/\Delta < 1-2\mu/\Delta$, consistently reproducing the result for the untilted Weyl semimetal.

D. The case of spin precession in the another plane

In this subsection, we investigate the current response when the spin precession occurs in the bc-plane, where $b, c \in \{x, y, z\}$. For instance, when the precession is confined to the yz-plane , i.e., $(b, c) = (y, z)$, the magnetization vector is given by $\boldsymbol{m}(t) = \left(\sqrt{1-m_\perp^2}, m_\perp \cos\Omega t, m_\perp \sin\Omega t\right)^T$. Correspondingly, the relevant subspace of the effective Floquet Hamiltonian takes the form

$$H'^{2\times 2}_{F,bc} = \begin{pmatrix} \epsilon'_1 + |\Omega| & -s\frac{A_5}{\sqrt{2}}(v^b_{12} - iv^c_{12}) \\ -s\frac{A_5}{\sqrt{2}}(v^b_{21} + iv^c_{21}) & \epsilon'_2 \end{pmatrix}. \tag{60}$$

The velocity operator along the a-direction is obtained by taking the momentum derivative of the Hamiltonian:

$$\tilde{v}'^{a;bc} = \begin{pmatrix} \partial_a\epsilon'_1 & -s\frac{A_5}{\sqrt{2}}((\partial_a v^b)_{12} - i(\partial_a v^c)_{12}) \\ -s\frac{A_5}{\sqrt{2}}((\partial_a v^b)_{21} + i(\partial_a v^c)_{21}) & \partial_a\epsilon'_2 \end{pmatrix}. \tag{61}$$

Following the same procedure as in Eqs. (34)–(36), the DC current induced by magnetization precession in the bc plane can be obtained by applying the cyclic permutation $(x, y, z) \to (a, b, c)$ to the full Hamiltonian, including the tilt term. Under this transformation, both $\bar{J}^{a;bc}_{\mathrm{shift}}$ and $\bar{J}^{a;bc}_{\mathrm{inj}}$ can be nonzero.

We now consider the dc current induced by magnetization precession in the yz plane for a Weyl system with a z-directed tilt. Here, each current denotes the sum of the contributions from the two Weyl nodes with opposite chiralities. After integration over the azimuthal angle ϕ, the potentially nonzero components are the shift current along the y direction, the circular injection current along the x direction, and the linear injection current along the

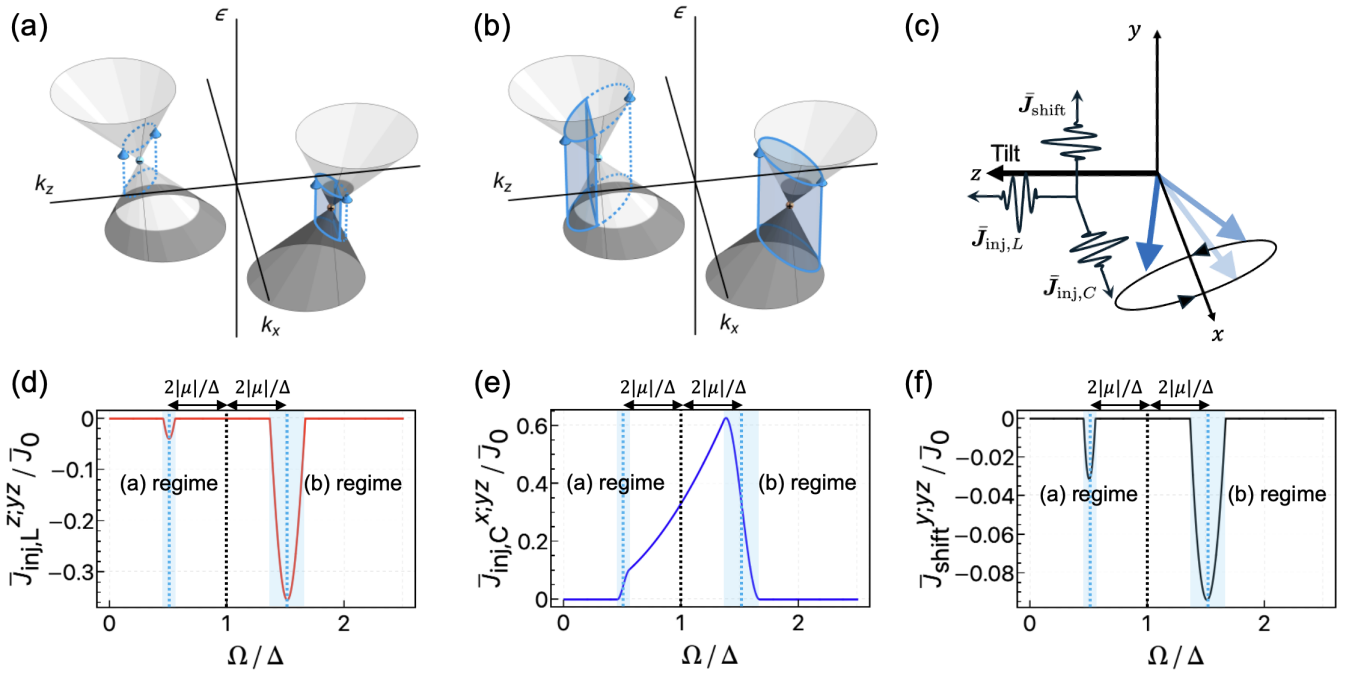


FIG. 5. Frequency dependence and directions of the dc currents induced by magnetization precession in the yz plane for a Weyl system with a z-directed tilt. (a) and (b) Schematics of the resonant interband transitions at the two Weyl nodes in the lower-frequency onset regime and the higher-frequency cancellation regime, respectively. The solid blue arrows represent Pauli-allowed transitions, whereas the dotted blue contours indicate the portions of the resonant surfaces excluded by Pauli blocking. The finite tilt makes the allowed transition phase space depend on k_z. (c) Relative directions of the tilt, magnetization precession, and the induced currents. The linear injection current is parallel to the tilt, $\bar{\boldsymbol{J}}_{{\rm inj},L} \parallel \boldsymbol{t}$; the circular injection current is parallel to the precession-helicity vector, $\bar{\boldsymbol{J}}_{{\rm inj},C} \parallel \boldsymbol{H}$; and the shift current is transverse to both, $\bar{\boldsymbol{J}}_{\rm shift} \parallel \boldsymbol{t} \times \boldsymbol{H}$, where $\boldsymbol{H} = i\boldsymbol{A}_{5,\Omega} \times \boldsymbol{A}^*_{5,\Omega}$. For the geometry shown here, these relations give $\bar{J}^{z;yz}_{{\rm inj},L}$, $\bar{J}^{x;yz}_{{\rm inj},C}$, and $\bar{J}^{y;yz}_{\rm shift}$. (d)–(f) Frequency dependences of the normalized linear injection current $\bar{J}^{z;yz}_{{\rm inj},L}/\bar{J}_0$, circular injection current $\bar{J}^{x;yz}_{{\rm inj},C}/\bar{J}_0$, and shift current $\bar{J}^{y;yz}_{\rm shift}/\bar{J}_0$, respectively, where $\bar{J}_0 = \Delta A_5^2/(2\pi)$. The blue dotted vertical lines mark $\Omega/\Delta = 1 - 2|\mu|/\Delta$ and $\Omega/\Delta = 1 + 2|\mu|/\Delta$, while the black dotted line marks $\Omega/\Delta = 1$. We set $\tau\Delta = 1.0$. The horizontal arrows indicate the separation $2|\mu|/\Delta$ between these characteristic frequencies. The light-blue shaded regions denote the frequency windows broadened by the finite Weyl-cone tilt and correspond to the regimes illustrated in panels (a) and (b). In the present geometry, the linear shift current vanishes, so that the shift current shown in panel (f) is entirely helicity odd.

z direction:

$$\bar{J}^{y;yz}_{\rm shift} = 2\cdot\frac{\Omega A_5^2}{16\pi}\int_{-\bar{k}}^{\min\{\bar{k},K_+\}}\frac{dk_z}{\bar{k}}\frac{k_z}{\bar{k}} - \frac{\Omega A_5^2}{16\pi}\int_{\max\{-\bar{k},K_-\}}^{\min\{\bar{k},K_+\}}\frac{dk_z}{\bar{k}}\frac{k_z}{\bar{k}}, \tag{62}$$

$$\bar{J}^{x;yz}_{{\rm inj},C} = \tau\frac{\Omega^2 A_5^2}{8\pi}\int_{\max\{-\bar{k},K_-\}}^{\min\{\bar{k},K_+\}}\frac{dk_z}{\bar{k}}\left[1-\left(\frac{k_z}{\bar{k}}\right)^2\right], \tag{63}$$

$$\bar{J}^{z;yz}_{{\rm inj},L} = 2\tau\frac{\Omega^2 A_5^2}{16\pi}\int_{-\bar{k}}^{\min\{\bar{k},K_+\}}\frac{dk_z}{\bar{k}}\frac{k_z}{\bar{k}}\left[3-\left(\frac{k_z}{\bar{k}}\right)^2\right] - \tau\frac{\Omega^2 A_5^2}{16\pi}\int_{\max\{-\bar{k},K_-\}}^{\min\{\bar{k},K_+\}}\frac{dk_z}{\bar{k}}\frac{k_z}{\bar{k}}\left[3-\left(\frac{k_z}{\bar{k}}\right)^2\right]. \tag{64}$$

The integrals are understood to vanish when their lower boundary is greater than or equal to their upper boundary (see Fig. 5).

The directions of these current components can be understood as follows. The linear injection current is even under reversal of the magnetization-precession direction. For the isotropic Weyl model with a z-directed tilt, azimuthal integration eliminates the x and y components, leaving only the component parallel to the tilt direction, $\bar{\boldsymbol{J}}_{{\rm inj},L} \parallel \boldsymbol{t}$. Since the electric current is a polar vector while the symmetric quadratic combination of the driving fields is inversion even, a nonzero net linear injection current requires inequivalent contributions from inversion-related Weyl nodes. In an inversion-symmetric system, their contributions cancel.

The circular injection current is odd under reversal of the magnetization-precession direction and flows along the spin-helicity vector $\boldsymbol{H} \equiv i\boldsymbol{A}_{5,\Omega} \times \boldsymbol{A}^*_{5,\Omega}$. For precession in the yz plane, $\boldsymbol{H}$ points along the x direction. More precisely, the antisymmetric part of the driving-field bilinear couples to the Berry curvature, producing a circular injection current along $\boldsymbol{H}$. Because the Berry curvature changes sign between Weyl nodes of opposite chiralities, their circular injection currents are oppositely directed. A finite total current therefore requires unequal

transition phase spaces at the two Weyl nodes.

The shift current is a polar vector and is odd under spatial inversion. The helicity $\boldsymbol{H}$ is an axial vector, whereas the tilt $\boldsymbol{t}$ is a polar vector. Therefore, $\boldsymbol{t}\times\boldsymbol{H}$ transforms as a polar vector:

$$\mathcal{P}:\boldsymbol{t}\mapsto-\boldsymbol{t},\ \boldsymbol{H}\mapsto\boldsymbol{H},\ \boldsymbol{t}\times\boldsymbol{H}\mapsto-\boldsymbol{t}\times\boldsymbol{H}. \tag{65}$$

The symmetry-allowed direction of the shift current is therefore $\bar{\boldsymbol{J}}_{\rm shift}\parallel\boldsymbol{t}\times\boldsymbol{H}$. For a z-directed tilt and yz-plane precession, $\boldsymbol{t}\parallel\hat{\boldsymbol{z}}$ and $\boldsymbol{H}\parallel\hat{\boldsymbol{x}}$, so that $\bar{\boldsymbol{J}}_{\rm shift}\parallel\hat{\boldsymbol{y}}$, up to the sign of the microscopic response coefficient [33, 37].

E. Direction of the Current Response

In the preceding analysis, we focused on a fixed direction of the magnetization precession. To discuss the reversal of the precession direction, we separate the magnitude and direction of the frequency by introducing $\eta\equiv\mathrm{sgn}(\Omega)$ and $\Omega=\eta|\Omega|$. For the magnetization precession in the yz plane, we write $\boldsymbol{m}(t)=\left(\sqrt{1-m_\perp^2},m_\perp\cos|\Omega|t,\eta m_\perp\sin|\Omega|t\right)^T$. With this convention, the resonant Floquet subspace is always constructed from the one-photon-dressed valence band and the bare conduction band, irrespective of the sign of Ω. The corresponding effective Floquet Hamiltonian is

$$H_{F,\eta}^{2\times2}=\begin{pmatrix}\epsilon_1+|\Omega| & -s\frac{A_5}{\sqrt{2}}\left(v_{12}^y-i\eta v_{12}^z\right)\\ -s\frac{A_5}{\sqrt{2}}\left(v_{21}^y+i\eta v_{21}^z\right) & \epsilon_2\end{pmatrix}. \tag{66}$$

We define

$$R_{12,\eta}^{a;yz}\equiv\partial_a\arg\left(v_{12}^y+i\eta v_{12}^z\right)+\mathcal{A}_{11}^a-\mathcal{A}_{22}^a. \tag{67}$$

It then follows that $R_{12,-\eta}^{a;zy}=R_{12,\eta}^{a;yz}$. Note that the off-diagonal Floquet matrix element for a given precession helicity η is proportional to $v_{12}^y-i\eta v_{12}^z$. According to the above definition, the corresponding shift vector is therefore $R_{12,-\eta}^{a;yz}$.

The reversal of the precession direction is related to the symmetric and antisymmetric decomposition with respect to the two driving indices. The symmetric and antisymmetric parts of either the injection or shift current can equivalently be obtained from the currents for the two opposite precession directions:

$$\bar{J}_{X,L}^{a;yz}=\frac{\bar{J}_{X,+}^{a;yz}+\bar{J}_{X,-}^{a;yz}}{2},\ \bar{J}_{X,C}^{a;yz}=\frac{\bar{J}_{X,+}^{a;yz}-\bar{J}_{X,-}^{a;yz}}{2}, \tag{68}$$

where $X=\mathrm{inj},\mathrm{shift}$ and the subscripts $\pm$ denote $\eta=\pm1$, respectively.

For the injection current, this decomposition is particularly transparent in terms of the quantum geometric tensor. The quantum-metric contribution is symmetric under the interchange of the two driving indices, whereas the Berry-curvature contribution is antisymmetric. Accordingly,

$$\left(v_{11}^a-v_{22}^a\right)\left(\mathcal{G}_{12}^{yy}+\mathcal{G}_{12}^{zz}\right)\to\left(v_{11}^a-v_{22}^a\right)\left(\mathcal{G}_{12}^{yy}+\mathcal{G}_{12}^{zz}\right), \tag{69}$$

$$\left(v_{11}^a-v_{22}^a\right)\mathcal{F}_{12}^{yz}\to\eta\left(v_{11}^a-v_{22}^a\right)\mathcal{F}_{12}^{yz}. \tag{70}$$

Thus, the linear injection current is even under $\eta\to-\eta$, while the circular injection current is odd:

$$\bar{J}_{\rm inj,L}^{z;yz}(-\eta)=\bar{J}_{\rm inj,L}^{z;yz}(\eta),\quad \bar{J}_{\rm inj,C}^{z;yz}(-\eta)=-\bar{J}_{\rm inj,C}^{z;yz}(\eta). \tag{71}$$

For the shift current, however, the precession dependence cannot be determined from the quantum metric and Berry curvature alone, because the shift vector itself depends on the precession helicity. The shift vector associated with the Floquet matrix element $v_{12}^y-i\eta v_{12}^z$ is $R_{12,-\eta}^{a;yz}$. Therefore, the relevant helicity-dependent combination is

$$\left|v_{12}^y-iv_{12}^z\right|^2R_{12,-}^{a;yz}\to\left|v_{12}^y-i\eta v_{12}^z\right|^2R_{12,-\eta}^{a;yz}. \tag{72}$$

Although the velocity matrix element can be written as

$$\left|v_{12}^y-i\eta v_{12}^z\right|^2=(\epsilon_{12})^2\left(\mathcal{G}_{12}^{yy}+\mathcal{G}_{12}^{zz}-\eta\mathcal{F}_{12}^{yz}\right), \tag{73}$$

the factors proportional to the quantum metric and Berry curvature cannot be separately identified with the linear and circular shift currents before the η dependence of $R_{12,-\eta}^{a;yz}$ is included. For the present Weyl Hamiltonian, the direct evaluation of Eq. (72) gives, after the azimuthal integration,

$$\bar{J}_{\rm shift,-}^{y;yz}=-\bar{J}_{\rm shift,+}^{y;yz}. \tag{74}$$

Consequently,

$$\bar{J}_{\rm shift,L}^{y;yz}=0,\quad \bar{J}_{\rm shift,C}^{y;yz}=\bar{J}_{\rm shift,+}^{y;yz}=-\bar{J}_{\rm shift,-}^{y;yz}. \tag{75}$$

Therefore, the finite shift current obtained for the yz-plane precession is purely antisymmetric with respect to the two driving indices and reverses its direction when the sense of magnetization precession is reversed.

Note that the operation changing sign of η correspond exchanging subscripts of input.

IV. NUMERICAL CALCULATION

To estimate the magnitude of these current density in a realistic MWSM accessible to experiment, we consider the compensated ferrimagnetic inverse-Heusler compound Ti_2MnAl, which has been predicted to host Weyl nodes near the Fermi energy [38]. Its compensated ferrimagnetic order breaks $\mathcal{T}$ symmetry, and its noncentrosymmetric crystal structure breaks $\mathcal{P}$ symmetry. These band-structure and symmetry properties motivate the application of the continuum-model analysis.

An effective tight-binding study of Ti_2MnAl indicates strong exchange coupling between the Ti and Mn sublattices, together with weak magnetic anisotropy of the

ferrimagnetic order [39–41]. These results motivate a quantitative investigation of spin precession driven by an oscillating magnetic field. In the following, we solve the coupled Landau–Lifshitz–Gilbert equations to determine the resonance frequency and precession amplitude, which we then use to estimate the induced current density.

A. Landau–Lifshitz–Gilbert Equation of Ti_2MnAl

We use the 4×4 model of Ref. [42], with unit magnetization vectors satisfying $|\boldsymbol{m}^a| = 1$. At Weyl nodes $\boldsymbol{k} = \boldsymbol{k}_W$, the Hamiltonian is

$$H_{\mathrm{TMA}}(\boldsymbol{k}; \boldsymbol{m}^{\mathrm{Ti1}}, \boldsymbol{m}^{\mathrm{Mn}}) = \begin{pmatrix} \xi_{\mathrm{Ti1}} I_2 + \boldsymbol{b}_{\mathrm{Ti1}} \cdot \boldsymbol{\sigma} & (d_1 - id_2) I_2 \\ (d_1 + id_2) I_2 & \xi_{\mathrm{Mn}} I_2 + \boldsymbol{b}_{\mathrm{Mn}} \cdot \boldsymbol{\sigma} \end{pmatrix}, \tag{76}$$

where

$$\xi_a(\boldsymbol{k}) = \epsilon_a - 2t_{aa} f(\boldsymbol{k}), \quad a = \mathrm{Ti1},\ \mathrm{Mn}, \tag{77}$$

$$\boldsymbol{b}_{\mathrm{Ti1}}(\boldsymbol{k}) = -J^{\mathrm{Ti1}}_{\mathrm{exc}} \boldsymbol{m}^{\mathrm{Ti1}} - 2\lambda_{\mathrm{Ti1}} \boldsymbol{n}_{\mathrm{KM}}(\boldsymbol{k}), \tag{78}$$

$$\boldsymbol{b}_{\mathrm{Mn}}(\boldsymbol{k}) = -J^{\mathrm{Mn}}_{\mathrm{exc}} \boldsymbol{m}^{\mathrm{Mn}} + 2\lambda_{\mathrm{Mn}} \boldsymbol{n}_{\mathrm{KM}}(\boldsymbol{k}), \tag{79}$$

$$d_1(\boldsymbol{k}) = -2t_{\mathrm{Mn,Ti1}} \sum_{i=x,y,z} \cos\frac{k_i}{2} - 4\big(t_{\mathrm{Ti1,Ti2,Mn}} + t_{\mathrm{Ti1,Al,Mn}}\big) \prod_{i=x,y,z} \cos\frac{k_i}{2}, \tag{80}$$

$$d_2(\boldsymbol{k}) = 4\big(t_{\mathrm{Ti1,Ti2,Mn}} - t_{\mathrm{Ti1,Al,Mn}}\big) \prod_{i=x,y,z} \sin\frac{k_i}{2}. \tag{81}$$

Here, we use the parameter values [42]:

$$\begin{aligned} \epsilon_{\mathrm{Ti1}} &= 1.1074\ \mathrm{eV}, \quad \epsilon_{\mathrm{Mn}} = -0.5066\ \mathrm{eV}, \\ J^{\mathrm{Ti1}}_{\mathrm{exc}} &= 1.6154\ \mathrm{eV}, \quad J^{\mathrm{Mn}}_{\mathrm{exc}} = 0.7836\ \mathrm{eV}, \\ \lambda_{\mathrm{Ti1}} &= \lambda_{\mathrm{Mn}} = 0.015\ \mathrm{eV}, \\ t_{\mathrm{Ti1,Ti1}} &= 0.1768\ \mathrm{eV}, \quad t_{\mathrm{Mn,Mn}} = -0.102\ \mathrm{eV}, \\ t_{\mathrm{Mn,Ti1}} &= -0.0544\ \mathrm{eV}, \\ t_{\mathrm{Ti1,Ti2,Mn}} &= 0.076\ \mathrm{eV}, \quad t_{\mathrm{Ti1,Al,Mn}} = 0.05\ \mathrm{eV}. \end{aligned} \tag{82}$$

The dimensionless hopping and spin-orbit coupling (SOC) structure factors are

$$f(\boldsymbol{k}) = 2\left(\cos\frac{k_x}{2}\cos\frac{k_y}{2} + \cos\frac{k_y}{2}\cos\frac{k_z}{2} + \cos\frac{k_z}{2}\cos\frac{k_x}{2}\right), \tag{83}$$

$$\boldsymbol{n}_{\mathrm{KM}}(\boldsymbol{k}) = -\sqrt{2} \begin{pmatrix} \sin\frac{k_x}{2}\left(\cos\frac{k_y}{2} - \cos\frac{k_z}{2}\right) \\ \sin\frac{k_y}{2}\left(\cos\frac{k_z}{2} - \cos\frac{k_x}{2}\right) \\ \sin\frac{k_z}{2}\left(\cos\frac{k_x}{2} - \cos\frac{k_y}{2}\right) \end{pmatrix}. \tag{84}$$

The components of $\boldsymbol{k}$ refer to the cubic crystal axes, with the lattice constant set to unity. The four band energies, labeled by $\nu = 1, \ldots, 4$, satisfy

$$\det[E_\nu(\boldsymbol{k}; \boldsymbol{m}^{\mathrm{Ti1}}, \boldsymbol{m}^{\mathrm{Mn}}) I_4 - H_{\mathrm{TMA}}(\boldsymbol{k}; \boldsymbol{m}^{\mathrm{Ti1}}, \boldsymbol{m}^{\mathrm{Mn}})] = 0. \tag{85}$$

Their grand canonical potential per primitive cell is

$$\Phi_{\mathrm{el}}(\boldsymbol{m}^{\mathrm{Ti1}}, \boldsymbol{m}^{\mathrm{Mn}}) \equiv -\frac{k_{\mathrm{B}}T}{N_k} \sum_{\boldsymbol{k},\nu} \log(1 + e^{-[E_\nu(\boldsymbol{k}; \boldsymbol{m}^{\mathrm{Ti1}}, \boldsymbol{m}^{\mathrm{Mn}}) - \mu]\beta}), \tag{86}$$

where β is the inverse temperature $(k_{\mathrm{B}}T)^{-1}$ and N_k is the number of sampled wave vectors. The electron number within this model is

$$n_e \equiv \frac{1}{N_k} \sum_{\boldsymbol{k},\nu} \frac{1}{1 + e^{[E_\nu(\boldsymbol{k}; \boldsymbol{m}^{\mathrm{Ti1}}, \boldsymbol{m}^{\mathrm{Mn}}) - \mu]\beta}}. \tag{87}$$

The electronic free energy is

$$F_{\mathrm{el}} \equiv \Phi_{\mathrm{el}} + \mu n_e = \Phi_0 + \frac{1}{2}\delta\boldsymbol{m}^T C \delta\boldsymbol{m} + \mathcal{O}(|\delta\boldsymbol{m}|^3) + \mu n_e, \tag{88}$$

where $\delta\boldsymbol{m} = (0, m_y^{\mathrm{Ti1}}, m_z^{\mathrm{Ti1}}, 0, m_y^{\mathrm{Mn}}, m_z^{\mathrm{Mn}})^T$. We expand on $\boldsymbol{m}^{\mathrm{Ti1}} = -\boldsymbol{m}^{\mathrm{Mn}} = \hat{\boldsymbol{x}}$, with $\hat{\boldsymbol{x}} \parallel [111]$, $\hat{\boldsymbol{y}} \parallel [1\bar{1}0]$, and $\hat{\boldsymbol{z}} = \hat{\boldsymbol{x}} \times \hat{\boldsymbol{y}}$, keeping each vector normalized. At fixed $\mu = 0$, $k_{\mathrm{B}}T = 10$ meV, and $N_k = 128^3$, we obtain $n_e = 2.00135$ and

$$C = \begin{pmatrix} 0 & 0 & 0 & 0 & 0 & 0 \\ 0 & 28.5498 & 0 & 0 & 28.5435 & 0 \\ 0 & 0 & 28.5498 & 0 & 0 & 28.5435 \\ 0 & 0 & 0 & 0 & 0 & 0 \\ 0 & 28.5435 & 0 & 0 & 28.5552 & 0 \\ 0 & 0 & 28.5435 & 0 & 0 & 28.5552 \end{pmatrix}, \tag{89}$$

in meV per cell, where $C_{ij} = \partial_i \partial_j \Phi_{\mathrm{el}}|_{\delta\boldsymbol{m}=0}$. With $\delta\boldsymbol{m}^a = (m_y^a, m_z^a)$,

$$\begin{aligned} F_0 =& \mathcal{J}\boldsymbol{m}^{\mathrm{Ti1}} \cdot \boldsymbol{m}^{\mathrm{Mn}} - \frac{K_{\mathrm{Ti1}}}{2}(m_x^{\mathrm{Ti1}})^2 - \frac{K_{\mathrm{Mn}}}{2}(m_x^{\mathrm{Mn}})^2 \\ \approx& -\mathcal{J} - \frac{K_{\mathrm{Ti1}}}{2} - \frac{K_{\mathrm{Mn}}}{2} \\ &+ \frac{\mathcal{J} + K_{\mathrm{Ti1}}}{2}|\delta\boldsymbol{m}^{\mathrm{Ti1}}|^2 + \frac{\mathcal{J} + K_{\mathrm{Mn}}}{2}|\delta\boldsymbol{m}^{\mathrm{Mn}}|^2 \\ &+ \mathcal{J}\delta\boldsymbol{m}^{\mathrm{Ti1}} \cdot \delta\boldsymbol{m}^{\mathrm{Mn}}. \end{aligned} \tag{90}$$

Thus $\mathcal{J} = C_{25} = C_{36}$, $K_{\mathrm{Ti1}} = C_{22} - \mathcal{J}$, and $K_{\mathrm{Mn}} = C_{55} - \mathcal{J}$ give

$$\mathcal{J} = 28.5435\ \mathrm{meV}, \tag{91}$$

$$K_{\mathrm{Ti1}} = 6.2997\ \mu\mathrm{eV}, \tag{92}$$

$$K_{\mathrm{Mn}} = 11.6624\ \mu\mathrm{eV}, \tag{93}$$

per cell; the two anisotropies are kept distinct. For $\boldsymbol{B}_{\mathrm{ext}} = B_{\mathrm{ac}}(0, -\sin\Omega t, \cos\Omega t)$, we solve the coupled LLG equations

$$\dot{\boldsymbol{m}}^a = -\gamma \boldsymbol{m}^a \times \boldsymbol{B}^a_{\mathrm{eff}} + \alpha \boldsymbol{m}^a \times \dot{\boldsymbol{m}}^a, \tag{94}$$

$$\boldsymbol{B}^a_{\mathrm{eff}} = \boldsymbol{B}_{\mathrm{ext}} - \frac{1}{\mu^a}\frac{\partial F_0}{\partial \boldsymbol{m}^a}. \tag{95}$$

Setting $\boldsymbol{n} \equiv (\boldsymbol{m}^{\mathrm{Ti1}} - \boldsymbol{m}^{\mathrm{Mn}})/2$, $\boldsymbol{N} \equiv (\boldsymbol{m}^{\mathrm{Ti1}} + \boldsymbol{m}^{\mathrm{Mn}})/2$, and linearizing about the antiparallel state, we use

$$u \equiv n_y + i n_z = u_\Omega e^{i\Omega t}, \tag{96}$$

$$v \equiv N_y + i N_z = v_\Omega e^{i\Omega t}. \tag{97}$$

The numerical steady-state solution thus gives

$$n_\perp \equiv |u_\Omega| = 2.63519 \times 10^{-3}, \tag{98}$$

$$\Omega_{\mathrm{res}} = 8.364 \times 10^{11}\ \mathrm{rad/s}, \tag{99}$$

where Ω_{res} maximizes $n_\perp$ for the stated rotation direction. Note that $\Omega_{\mathrm{res}}/2\pi = 133.12$ GHz. We use $\gamma = 2\mu_B/\hbar$ and $\mu^{\mathrm{Ti1}} = \mu^{\mathrm{Mn}} = 2.59\mu_B$, $\alpha = 0.01$, $B_{\mathrm{ac}} = 10$ mT [43].

B. Spin-Induced Current in Ti_2MnAl

In the sublattice basis, the exchange-coupling matrix is written as

$$\begin{aligned}\widehat{J} &= (J_0 - J_3)\frac{\tau_0 - \tau_3}{2} + (J_0 + J_3)\frac{\tau_0 + \tau_3}{2} \\ &\equiv J^{\mathrm{Ti1}}_{\mathrm{exc}}\frac{\tau_0 - \tau_3}{2} + J^{\mathrm{Mn}}_{\mathrm{exc}}\frac{\tau_0 + \tau_3}{2}.\end{aligned} \tag{100}$$

With $P_{\mathrm{Ti1}} = (\tau_0 - \tau_3)/2$ and $P_{\mathrm{Mn}} = (\tau_0 + \tau_3)/2$, the exchange Hamiltonian is

$$H_{\mathrm{exc}} = -\sum_{a=\mathrm{Ti1,Mn}} J^a_{\mathrm{exc}} P_a \otimes (\boldsymbol{m}^a \cdot \boldsymbol{\sigma}). \tag{101}$$

The parameter values in Eq. (82) give $J_0 = 1.1995$ eV and $J_3 = -0.4159$ eV.

For normalized spinors satisfying $(\boldsymbol{b}_a \cdot \boldsymbol{\sigma})\,|\chi_{a,\pm}\rangle = \pm|\boldsymbol{b}_a|\,|\chi_{a,\pm}\rangle$, the two degenerate states are

$$|u_1\rangle = \begin{pmatrix} |\chi_{\mathrm{Ti1},-}\rangle \\ \vec{0}_2 \end{pmatrix}, \quad |u_2\rangle = \begin{pmatrix} \vec{0}_2 \\ |\chi_{\mathrm{Mn},+}\rangle \end{pmatrix}, \tag{102}$$

where $\vec{0}_2$ is a 2×1 zero vector. Projecting onto this two-dimensional eigenspace gives

$$U^\dagger H_{\mathrm{TMA}}(\boldsymbol{k}_W; \hat{\boldsymbol{x}}, -\hat{\boldsymbol{x}})U = \begin{pmatrix} E_W & 0 \\ 0 & E_W \end{pmatrix}, \tag{103}$$

where the 4×2 matrix

$$U = \begin{pmatrix} |\chi_{\mathrm{Ti1},-}\rangle & \vec{0}_2 \\ \vec{0}_2 & |\chi_{\mathrm{Mn},+}\rangle \end{pmatrix} \tag{104}$$

satisfies $U^\dagger U = I_2$, and the Weyl-node energy is

$$E_W = \xi_{\mathrm{Ti1}} - |\boldsymbol{b}_{\mathrm{Ti1}}| = \xi_{\mathrm{Mn}} + |\boldsymbol{b}_{\mathrm{Mn}}|. \tag{105}$$

To extract the Néel coupling, take $\delta\boldsymbol{N} = 0$. With $\boldsymbol{q} = \boldsymbol{k} - \boldsymbol{k}_W$ and the fixed equilibrium basis U, the time-dependent model to first order in $\boldsymbol{q}$ and $\delta\boldsymbol{n} = (0, \delta n_y, \delta n_z)^T$ is

$$\begin{aligned}H_{\boldsymbol{k}\cdot\boldsymbol{p}} &\equiv U^\dagger H_{\mathrm{TMA}}(\boldsymbol{k}_W + \boldsymbol{q}; \boldsymbol{m}^{\mathrm{Ti1}}, \boldsymbol{m}^{\mathrm{Mn}})U \\ &\approx E_W I_2 + \sum_i q_i U^\dagger(\partial_{k_i} H_0)U + \sum_{\beta=y,z} \delta n_\beta(t)\Gamma_\beta,\end{aligned} \tag{106}$$

where $H_0(\boldsymbol{k}) = H_{\mathrm{TMA}}(\boldsymbol{k}; \hat{\boldsymbol{x}}, -\hat{\boldsymbol{x}})$ and all derivatives are evaluated at $\boldsymbol{k}_W$. The exchange vertices are

$$\begin{aligned}\Gamma_\beta &\equiv U^\dagger \begin{pmatrix} -J^{\mathrm{Ti1}}_{\mathrm{exc}}\sigma_\beta & 0 \\ 0 & +J^{\mathrm{Mn}}_{\mathrm{exc}}\sigma_\beta \end{pmatrix} U \\ &= \begin{pmatrix} \mathrm{Tr}[\Gamma_\beta/2] + J^{\mathrm{eff}}_{\mathrm{exc},\beta} & 0 \\ 0 & \mathrm{Tr}[\Gamma_\beta/2] - J^{\mathrm{eff}}_{\mathrm{exc},\beta} \end{pmatrix},\end{aligned} \tag{107}$$

$$J^{\mathrm{eff}}_{\mathrm{exc},\beta} \equiv \frac{J^{\mathrm{Ti1}}_{\mathrm{exc}}\hat{b}_{\mathrm{Ti1},\beta} - J^{\mathrm{Mn}}_{\mathrm{exc}}\hat{b}_{\mathrm{Mn},\beta}}{2}, \tag{108}$$

where $\hat{\boldsymbol{b}}_a = \boldsymbol{b}_a/|\boldsymbol{b}_a|$.

For $\hat{\boldsymbol{x}} \parallel [111]$, $\hat{\boldsymbol{y}} \parallel [1\bar{1}0]$, $\hat{\boldsymbol{z}} = \hat{\boldsymbol{x}} \times \hat{\boldsymbol{y}}$, we choose

$$\frac{\boldsymbol{k}_W}{2\pi} = (-0.7641737293, -0.5188957639, 0) \tag{109}$$

in cubic crystal coordinates with lattice constant set to unity. We obtain $E_W = -1.89413$ meV and

$$\begin{pmatrix} J^{\mathrm{eff}}_{\mathrm{exc},x} \\ J^{\mathrm{eff}}_{\mathrm{exc},y} \\ J^{\mathrm{eff}}_{\mathrm{exc},z} \end{pmatrix} = \begin{pmatrix} 0 \\ 0.0716059 \\ -0.0172105 \end{pmatrix}\ \mathrm{eV}. \tag{110}$$

Therefore, defining the effective exchange coupling as the maximum coupling to a unit transverse displacement,

$$\begin{aligned}J^{\mathrm{eff}}_{\mathrm{exc}} &\equiv \sqrt{(J^{\mathrm{eff}}_{\mathrm{exc},x})^2 + (J^{\mathrm{eff}}_{\mathrm{exc},y})^2 + (J^{\mathrm{eff}}_{\mathrm{exc},z})^2} \\ &= 0.0736452\ \mathrm{eV}.\end{aligned} \tag{111}$$

For circular Néel precession of amplitude $n_\perp$, the length of the axial gauge field is $J^{\mathrm{eff}}_{\mathrm{exc}} n_\perp/(\sqrt{2}v)$.

C. Estimation of the Spin-Induced Current

We estimate a reference current scale using a single tilted Weyl cone with an isotropic exchange approximation. We use the magnitude $J^{\mathrm{eff}}_{\mathrm{exc}}$ obtained above and identify $m_\perp = n_\perp$. The parameters are

$$\begin{aligned}&v = 6.0 \times 10^5\ \mathrm{m/s}, \quad J^{\mathrm{eff}}_{\mathrm{exc}} = 73.65\ \mathrm{meV}, \\ &n_\perp = 2.63519 \times 10^{-3}, \quad \tau = 1.0\ \mathrm{ps}, \quad \eta = +1, \\ &\hbar\Omega = 0.550528\ \mathrm{meV}, \quad \Gamma = \frac{\hbar}{2\tau} = 0.329106\ \mathrm{meV}.\end{aligned} \tag{112}$$

The corresponding chiral gauge-field amplitude is

$$A_5 = \frac{J^{\mathrm{eff}}_{\mathrm{exc}} n_\perp}{\sqrt{2}\hbar v} = 3.47498 \times 10^5\ \mathrm{m}^{-1}. \tag{113}$$

TABLE II. Correspondence between the electromagnetic gauge field and the chiral gauge field. The particle-current convention with $e = \hbar = 1$ is used. Here, $\int_{\boldsymbol{k}} \equiv \int \frac{d\boldsymbol{k}}{(2\pi)^3}$ and $\mathcal{Q}^{xy}_{12} \equiv \mathcal{G}^{xx}_{12} + \mathcal{G}^{yy}_{12} - \mathcal{F}^{xy}_{12}$. The optical formulas have been rewritten in the particle-current convention and in the relaxation-time convention used in this work.

	Electromagnetic gauge field [33, 37, 44]	Chiral gauge field (our work)
	$\boldsymbol{A}_\Omega = A(1,i,0)^T,\ \boldsymbol{E}_\Omega = i\Omega\boldsymbol{A}_\Omega,\ E \equiv \lvert\boldsymbol{E}_\Omega\rvert = \sqrt{2}\Omega A$	$\boldsymbol{A}_{5,\Omega} = \frac{A_5}{\sqrt{2}}(1,i,0)^T,\ A_5 = \frac{J_{\rm exc} m_\perp}{\sqrt{2}v},\ E_5 \equiv \Omega A_5$
Injection	$\bar{J}^{a;xy}_{\rm inj}(E) = 4\pi\tau E^2 \int_{\boldsymbol{k}} f_{12}(v^a_{11} - v^a_{22})\mathcal{Q}^{xy}_{12}\delta(\epsilon_{12}+\Omega)$	$\bar{J}^{a;xy}_{\rm inj}(A_5) = 2\pi\tau E_5^2 \int_{\boldsymbol{k}} f_{12}(v^a_{11} - v^a_{22})\mathcal{Q}^{xy}_{12}\delta(\epsilon_{12}+\Omega)$
Shift	$\bar{J}^{a;xy}_{\rm shift}(E) = 2\pi E^2 \int_{\boldsymbol{k}} f_{12} R^{a;xy}_{12,-}\mathcal{Q}^{xy}_{12}\delta(\epsilon_{12}+\Omega)$	$\bar{J}^{a;xy}_{\rm shift}(A_5) = \pi E_5^2 \int_{\boldsymbol{k}} f_{12} R^{a;xy}_{12,-}\mathcal{Q}^{xy}_{12}\delta(\epsilon_{12}+\Omega)$

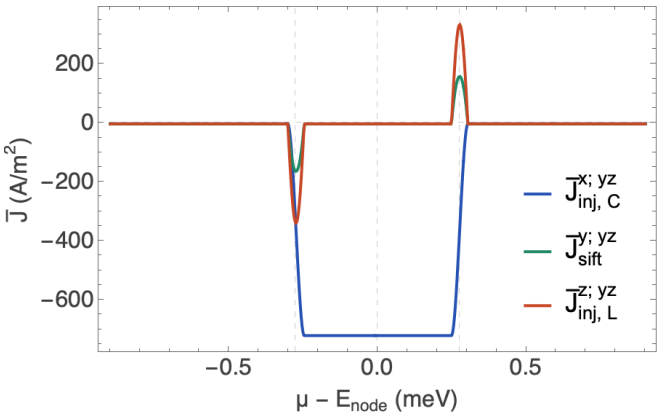


FIG. 6. Chemical-potential dependence of the spin-induced dc current density in the single-cone isotropic-exchange approximation for circular precession in the yz plane and a tilt along z. Blue, green, and red curves denote the circular-injection current $\bar{J}^{x;yz}_{{\rm inj},C}$, shift current $\bar{J}^{y;yz}_{\rm shift}$, and linear-injection current $\bar{J}^{z;yz}_{{\rm inj},L}$, respectively. The chemical potential is measured from the Weyl-node energy $E_{\rm node}$; the parameters are specified in the text.

Fig. 6 shows the chemical-potential dependence relative to the Weyl-node energy $E_{\rm node}$. The circular-injection current $\bar{J}^{x;yz}_{{\rm inj},C}$ reaches a negative plateau of approximately -7.2×10^2 A/m^2. The linear-injection and shift currents, $\bar{J}^{z;yz}_{{\rm inj},L}$ and $\bar{J}^{y;yz}_{\rm shift}$, have peak values of approximately $\pm 3.4 \times 10^2$ A/m^2 and $\pm 1.6 \times 10^2$ A/m^2, respectively, near $\mu - E_{\rm node} = \pm\hbar\Omega/2 = \pm 0.275264$ meV. Both are positive on the electron side and negative on the hole side.

These are formal second-order model estimates: the scalar approximation does not retain the rank-one projected coupling, and $J^{\rm eff}_{\rm exc} n_\perp/\Gamma \approx 0.590$ and $\Gamma/(\hbar\Omega) \approx 0.598$ do not establish a well-separated perturbative regime.

V. DISCUSSION

Let us discuss comparing our work with photoinduced currents. In noncentrosymmetric systems, nonlinear current responses induced by optical electric fields have been extensively investigated. The theoretical framework for these responses is now well established, and their topological and geometrical aspects have been clarified in terms of Berry curvature, Berry connection, and quantum metric [23, 35, 44–46]. In Weyl semimetals with broken $\mathcal{P}$ symmetry, which host topological Weyl nodes and exhibit large Berry curvature around these nodes, nonlinear responses have been well investigated and classified from the perspective of quantum geometry [33, 37]. While these geometric classifications are highly successful, they primarily consider conventional electromagnetic fields as the driving force. This phenomenon is prominent in MWSMs due to the strong exchange coupling between localized spins and conduction electrons. We find that the spin-induced response consists of a shift current proportional to Ω^1 and an injection current proportional to $\Omega^2\tau$, drawing a clear contrast to the low-frequency behavior of conventional photogalvanic effects [33, 44] (see Table II).

VI. SUMMARY

In this study, we evaluated the nonlinear DC current induced by steady spin precession in a simple model of a MWSM using the Floquet–Keldysh Green's function method. We showed that both circular shift and circular injection currents contribute to the response coefficient. In the untilted case, the total current from the two Weyl nodes exhibits discontinuous changes as a function of the driving frequency Ω. This behavior reflects three distinct regimes: (i) transitions at both nodes are forbidden because the final states lie below the chemical potential, resulting in zero current; (ii) transitions are allowed at both nodes, but their current contributions cancel exactly, also resulting in zero net current; and (iii) transitions are allowed at only one node, yielding a finite net current. Introducing a tilt to the Weyl cones causes the resonant surface to incline, so that transitions become allowed progressively as the driving frequency changes. Consequently, the discontinuous jumps observed in the untilted model are substantially smoothed out. Furthermore, when transitions are allowed over only part of the resonant surface because some initial states are unoccupied or some final states are occupied, the reduced sym-

metry of the tilted Weyl cones becomes particularly evident. In this regime, additional nonlinear current responses, including shift currents and linear injection currents, are allowed.

VII. ACKNOWLEDGMENTS

This work was supported by JSPS KAKENHI Grant Numbers JP24H00197, JP25H01250, JP26K00652, and JP26K00660.

[1] G. E. Volovik, Linear momentum in ferromagnets, J. Phys. C: Solid State Phys. **20**, L83 (1987).
[2] N. Nagaosa and Y. Tokura, Emergent electromagnetism in solids, Phys. Scr. **T146**, 014020 (2012).
[3] S. E. Barnes and S. Maekawa, Generalization of Faraday's law to include nonconservative spin forces, Phys. Rev. Lett. **98**, 246601 (2007).
[4] A. M. Essin, A. M. Turner, J. E. Moore, and D. Vanderbilt, Orbital magnetoelectric coupling in band insulators, Phys. Rev. B **81**, 205104 (2010).
[5] A. Harada and H. Ishizuka, Spin motive force by the momentum-space Berry phase in magnetic Weyl semimetals, Phys. Rev. B **107**, 195202 (2023).
[6] I. Žutić, J. Fabian, and S. Das Sarma, Spintronics: fundamentals and applications, Rev. Mod. Phys. **76**, 323 (2004).
[7] J. Puebla, J. Kim, K. Kondou, and Y. Otani, Spintronic devices for energy-efficient data storage and energy harvesting, Commun. Mater. **1**, 24 (2020).
[8] Y. Tserkovnyak, A. Brataas, and G. E. W. Bauer, Spin pumping and magnetization dynamics in metallic multilayers, Phys. Rev. B **66**, 224403 (2002).
[9] J. Varela-Manjarres, A. Kefayati, M. B. Jungfleisch, J. Q. Xiao, and B. K. Nikolić, Charge and spin current pumping by ultrafast demagnetization dynamics, Phys. Rev. B **110**, L060410 (2024).
[10] A. A. Burkov and L. Balents, Weyl semimetal in a topological insulator multilayer, Phys. Rev. Lett. **107**, 127205 (2011).
[11] X. Wan, A. M. Turner, A. Vishwanath, and S. Y. Savrasov, Topological semimetal and Fermi-arc surface states in the electronic structure of pyrochlore iridates, Phys. Rev. B **83**, 205101 (2011).
[12] N. P. Armitage, E. J. Mele, and A. Vishwanath, Weyl and Dirac semimetals in three-dimensional solids, Rev. Mod. Phys. **90**, 015001 (2018).
[13] Y. Araki, Magnetic textures and dynamics in magnetic Weyl semimetals, Ann. Phys. **532**, 1900287 (2020).
[14] N. Nagaosa, T. Morimoto, and Y. Tokura, Transport, magnetic and optical properties of Weyl materials, Nat. Rev. Mater. **5**, 621 (2020).
[15] P. Nikolić, Dynamics of local magnetic moments induced by itinerant Weyl electrons, Phys. Rev. B **103**, 155151 (2021).
[16] A. Ozawa, Y. Araki, K. Kobayashi, and K. Nomura, Magnetic Weyl semimetals: Interplay of band topology and magnetism (2026), arXiv:2603.22568 [cond-mat.mes-hall].
[17] T. Meguro, H. Ishizuka, and K. Nomura, Nonlinear spin-motive force driven by mixed-space quantum geometry (2026), arXiv:2603.11499 [cond-mat.mes-hall].
[18] H. Ishizuka, T. Hayata, M. Ueda, and N. Nagaosa, Emergent electromagnetic induction and adiabatic charge pumping in noncentrosymmetric Weyl semimetals, Phys. Rev. Lett. **117**, 216601 (2016).
[19] S. Kohler, J. Lehmann, and P. Hänggi, Driven quantum transport on the nanoscale, Physics Reports **406**, 379 (2005).
[20] A. Kamenev, *Field theory of non-equilibrium systems*, 2nd ed. (Cambridge University Press, 2023).
[21] T. Oka and H. Aoki, Photovoltaic hall effect in graphene, Physical Review B—Condensed Matter and Materials Physics **79**, 081406 (2009).
[22] H. Aoki, N. Tsuji, M. Eckstein, M. Kollar, T. Oka, and P. Werner, Nonequilibrium dynamical mean-field theory and its applications, Rev. Mod. Phys. **86**, 779 (2014).
[23] T. Morimoto and N. Nagaosa, Topological nature of nonlinear optical effects in solids, Sci. Adv. **2**, e1501524 (2016).
[24] O. Matsyshyn, F. Piazza, R. Moessner, and I. Sodemann, Rabi regime of current rectification in solids, Phys. Rev. Lett. **127**, 126604 (2021).
[25] B. Yan and C. Felser, Topological materials: Weyl semimetals, Annu. Rev. Condens. Matter Phys. **8**, 337 (2017).
[26] D. I. Pikulin, A. Chen, and M. Franz, Chiral anomaly from strain-induced gauge fields in Dirac and Weyl semimetals, Phys. Rev. X **6**, 041021 (2016).
[27] L. Liang, Current response to axial gauge fields in noncentrosymmetric magnetic Weyl semimetals, Phys. Rev. B **111**, L201109 (2025).
[28] S. Datta, Nanoscale device modeling: the Green's function method, Superlattices Microstruct. **28**, 253 (2000).
[29] A.-P. Jauho, N. S. Wingreen, and Y. Meir, Time-dependent transport in interacting and noninteracting resonant-tunneling systems, Phys. Rev. B **50**, 5528 (1994).
[30] J. H. Shirley, Solution of the Schr"odinger equation with a Hamiltonian periodic in time, Phys. Rev. **138**, B979 (1965).
[31] H. Sambe, Steady states and quasienergies of a quantum-mechanical system in an oscillating field, Phys. Rev. A **7**, 2203 (1973).
[32] B. M. Fregoso, Y. H. Wang, N. Gedik, and V. Galitski, Driven electronic states at the surface of a topological insulator, Phys. Rev. B **88**, 155129 (2013).
[33] J. Ahn, G.-Y. Guo, and N. Nagaosa, Low-frequency divergence and quantum geometry of the bulk photovoltaic effect in topological semimetals, Phys. Rev. X **10**, 041041 (2020).
[34] J. Ahn, G.-Y. Guo, N. Nagaosa, and A. Vishwanath, Riemannian geometry of resonant optical responses, Nat. Phys. **18**, 290 (2022).
[35] C.-K. Chan, N. H. Lindner, G. Refael, and P. A. Lee, Photocurrents in Weyl semimetals, Phys. Rev. B **95**, 041104(R) (2017).
[36] S. P. Mukherjee and J. P. Carbotte, Imaginary part of Hall conductivity in a tilted doped Weyl semimetal with

both broken time-reversal and inversion symmetry, Phys. Rev. B **97**, 035144 (2018).
[37] H. Watanabe and Y. Yanase, Chiral photocurrent in parity-violating magnet and enhanced response in topological antiferromagnet, Phys. Rev. X **11**, 011001 (2021).
[38] W. Shi, L. Muechler, K. Manna, Y. Zhang, K. Koepernik, R. Car, J. van den Brink, C. Felser, and Y. Sun, Prediction of a magnetic Weyl semimetal without spin-orbit coupling and strong anomalous Hall effect in the Heusler compensated ferrimagnet Ti2MnAl, Phys. Rev. B **97**, 060406(R) (2018).
[39] T. Meguro, A. Ozawa, K. Kobayashi, and K. Nomura, Effective tight-binding model of compensated ferrimagnetic Weyl semimetal with spontaneous orbital magnetization, J. Phys. Soc. Jpn. **93**, 034703 (2024).
[40] T. Meguro, A. Ozawa, K. Kobayashi, Y. Araki, and K. Nomura, Topological spin-orbit torque in ferrimagnetic weyl semimetal, Physical Review Research **7**, L022065 (2025).
[41] Y. Furusho, T. Meguro, and K. Nomura, Fermi arcs around magnetic domain walls in a compensated ferrimagnetic weyl semimetal ti2mnal, Journal of the Physical Society of Japan **94**, 064702 (2025).
[42] Y. Furusho, K. Kobayashi, and K. Nomura, In preparation.
[43] A. Jakobsson, P. Mavropoulos, E. Şaşıoğlu, S. Blügel, M. Ležaić, B. Sanyal, and I. Galanakis, First-principles calculations of exchange interactions, spin waves, and temperature dependence of magnetization in inverse-Heusler-based spin gapless semiconductors, Phys. Rev. B **91**, 174439 (2015).
[44] F. de Juan, A. G. Grushin, T. Morimoto, and J. E. Moore, Quantized circular photogalvanic effect in Weyl semimetals, Nat. Commun. **8**, 15995 (2017).
[45] J. E. Sipe and A. I. Shkrebtii, Second-order optical response in semiconductors, Phys. Rev. B **61**, 5337 (2000).
[46] I. Sodemann and L. Fu, Quantum nonlinear Hall effect induced by Berry curvature dipole in time-reversal invariant materials, Phys. Rev. Lett. **115**, 216806 (2015).

Appendix A: Floquet-Keldysh Formalism

To describe the nonequilibrium steady state, we employ the Floquet-Keldysh Green's function formalism.[20, 23, 24] Here, the operators $a^\dagger$ (a) and $b^\dagger$ (b) denote the creation (annihilation) operators for the system and the bath, respectively. As illustrated in Fig. 1(a), the total Hamiltonian of the system is given by

$$\mathcal{H}_{\rm tot}(t) = \mathcal{H}(t) + \mathcal{H}_{\rm bath} + \mathcal{H}_{\rm tun}, \tag{A1}$$

$$\mathcal{H}(t) = \sum_{\alpha\neq\beta} a^\dagger_\alpha \mathcal{H}^s_{\alpha\beta}(t) a_\beta = \mathcal{H}_0 + V(t), \tag{A2}$$

$$\mathcal{H}_{\rm bath} = \sum_\alpha \mathcal{E}^{\rm bath}_\alpha b^\dagger_\alpha b_\alpha, \tag{A3}$$

$$\mathcal{H}_{\rm tun} = \sum_{\alpha,\beta} (\mathcal{T}^\alpha b^\dagger_\alpha a_\beta + {\rm h.c.}), \tag{A4}$$

where the indices α and β denote the relevant band indices.

To formulate the problem using path integrals, we define the partition function and the corresponding action as

$$\mathcal{Z} = \int \mathcal{D}[a, a^\dagger, b, b^\dagger] e^{iS_{\rm tot}}, \tag{A5}$$

$$S_{\rm tot} = \int_C dt (\mathcal{L} + \mathcal{L}_{\rm bath} + \mathcal{L}_{\rm tun}), \tag{A6}$$

$$\mathcal{L} = \sum_{\alpha,\beta} a^\dagger_\alpha (i\partial_t - \mathcal{H}_{\alpha\beta}(t)) a_\beta, \tag{A7}$$

$$\mathcal{L}_{\rm bath} = \sum_\alpha b^\dagger_\alpha (i\partial_t - \mathcal{E}^{\rm bath}_\alpha) b_\alpha, \tag{A8}$$

$$\mathcal{L}_{\rm tun} = -\sum_{\alpha,\beta} (\mathcal{T}_\alpha b^\dagger_\alpha a_\beta + {\rm h.c.}), \tag{A9}$$

$$\langle b^\dagger_\alpha b_\alpha \rangle = f(\mathcal{E}^{\rm bath}_\alpha). \tag{A10}$$

Here, $\mathcal{E}^{\rm bath}_\alpha$ denotes the energy of bath state α. In the wide-band approximation, the bath-induced broadening is characterized by the relaxation rate Γ defined below.

1. Green's function

To systematically calculate the physical observables and correlation functions, we introduce the contour-ordered Green's functions via the generating functional approach.

We define the generating functional $W[\bar{J}, J, \bar{K}, K]$ by introducing auxiliary Grassmann source fields $\bar{J}, J$ that couple to the system operators $a, a^\dagger$, and $\bar{K}, K$ that couple to the bath operators $b, b^\dagger$:

$$e^{iW[\bar{J},J,\bar{K},K]} = \int \mathcal{D}[a,a^\dagger]\mathcal{D}[b,b^\dagger] \times \exp\left[iS - i\int_C dt \sum_\alpha \left(\bar{J}_\alpha a_\alpha + a^\dagger_\alpha J_\alpha + \bar{K}_\alpha b_\alpha + b^\dagger_\alpha K_\alpha\right)\right]. \tag{A11}$$

By taking the second functional derivatives of the generating functional with respect to these source fields and subsequently setting them to zero, we obtain the full interacting contour-ordered Green's functions for the system and the bath:

$$G^{\mu\nu}(t,t') = -i\frac{\delta^2 e^{iW[\bar{J},J,\bar{K},K]}}{\delta\bar{J}_\mu(t)\delta J_\nu(t')}\bigg|_{\bar{J},J,\bar{K},K=0} = -i\left\langle T_C a_\mu(t) a^\dagger_\nu(t')\right\rangle, \tag{A12}$$

$$G^{\mu\nu}_{\rm bath}(t,t') = -i\frac{\delta^2 e^{iW[\bar{J},J,\bar{K},K]}}{\delta\bar{K}_\mu(t)\delta K_\nu(t')}\bigg|_{\bar{J},J,\bar{K},K=0} = -i\left\langle T_C b_\mu(t) b^\dagger_\nu(t')\right\rangle. \tag{A13}$$

Here, T_C denotes the contour-ordering operator, which orders the field operators along the Keldysh contour C.

The expectation value $\langle(\cdots)\rangle$ with respect to the full action S is defined as

$$\langle(\cdots)\rangle = \frac{1}{\mathcal{Z}}\int \mathcal{D}[a,a^\dagger]\mathcal{D}[b,b^\dagger]e^{iS_{\rm tot}}(\cdots). \tag{A14}$$

Similarly, we define the unperturbed (bare) Green's functions by taking the expectation value with respect to the non-interacting action S_0 (i.e., the action decoupled from the tunneling Hamiltonian $\mathcal{H}_{\rm tun}$):

$$g^{\mu\nu}(t,t') = -i\left\langle T_C a_\mu(t)a_\nu^\dagger(t')\right\rangle_0, \tag{A15}$$

$$g_{\rm bath}^{\mu\nu}(t,t') = -i\left\langle T_C b_\mu(t)b_\nu^\dagger(t')\right\rangle_0, \tag{A16}$$

where the subscript 0 indicates that the path integral is performed using $S_0 = \int_C dt\sum_{\alpha,\beta} a_\alpha^\dagger(i\partial_t - \mathcal{H}_{0,\alpha\beta})a_\beta$:

$$\langle(\cdots)\rangle = \frac{1}{\mathcal{Z}}\int \mathcal{D}[a,a^\dagger]\mathcal{D}[b,b^\dagger]e^{iS_0}(\cdots). \tag{A17}$$

Depending on the relative positions of the time arguments t and t' on the forward or backward branches of the closed Keldysh contour, these contour-ordered Green's functions can be analytically continued into real-time components. This mapping naturally yields the lesser ($G^<$), greater ($G^>$), retarded (G^R), and advanced (G^A) Green's functions, which are essential for describing the non-equilibrium dynamics and spectral properties of the driven system.

2. Time Periodicity of the Action

Since the system Hamiltonian is time-periodic with period $T = 2\pi/\Omega$ such that $\mathcal{H}(t) = \mathcal{H}(t+T)$ due to the external driving $V(t) = V(t+T)$, we can expand it as a discrete Fourier series:

$$\mathcal{H}_{\alpha\beta}(t) = \sum_{m=-\infty}^{\infty} H_m^{\alpha\beta}e^{-im\Omega t}, \tag{A18}$$

$$H_m^{\alpha\beta} = \int_0^T \frac{dt}{T}e^{+im\Omega t}\mathcal{H}^{\alpha\beta}(t), \tag{A19}$$

where the field operators are expressed in the Schrödinger picture. By introducing the continuous Fourier transforms for these operators,

$$a_\alpha^\dagger(t) = \int\frac{d\omega}{2\pi}e^{i\omega t}a_\alpha^\dagger(\omega), \quad a_\beta(t) = \int\frac{d\omega'}{2\pi}e^{-i\omega' t}a_\beta(\omega'), \tag{A20}$$

the action can be expanded and transformed into the frequency-space representation. Noting that the time integration is performed over the Keldysh contour C, the field operators implicitly carry the Keldysh branch indices (+ and −). To express the action in the Floquet basis, we fold the frequency integral into the Floquet Brillouin zone $[0,\Omega)$ using the relation:

$$\int_{-\infty}^{\infty}d\omega\chi(\omega) = \sum_{n=-\infty}^{\infty}\int_0^\Omega d\omega\chi(\omega+n\Omega), \tag{A21}$$

where $\chi(\omega)$ is an arbitrary function. By applying this identity and introducing the Floquet component notation $a_{\alpha,n}^{(\dagger)}(\omega) \equiv a_\alpha^{(\dagger)}(\omega+n\Omega)$, the action is rewritten as

$$\begin{aligned} S &= \int_C dt\sum_{\alpha,\beta}a_\alpha^\dagger(i\partial_t - \sum_m H_m^{\alpha\beta}e^{-im\Omega t})a_\beta \\ &= \sum_{\alpha,\beta}\sum_{l,n}\int_0^\Omega d\omega\, a_{\alpha,n}^\dagger(\omega)\Big(\omega\delta_{l,n} - (H_F^{\alpha\beta})_{n,l}\Big)a_{\beta,l}(\omega), \end{aligned} \tag{A22}$$

where we have shifted the summation index to $l = m+n$ and defined the Floquet Hamiltonian matrix elements as

$$(H_F^{\alpha\beta})_{n,l} \equiv H_{l-n}^{\alpha\beta} - n\Omega\delta_{l,n}. \tag{A23}$$

Similarly, the actions for the tunneling coupling and the bath can be transformed into the Floquet basis:

$$S_{\rm tnn} = \sum_{\alpha,\beta}\sum_n\int_0^\Omega d\omega\mathcal{T}_\alpha b_{\alpha,n}^\dagger(\omega)a_{\beta,n}(\omega) + \text{h.c.}, \tag{A24}$$

$$\begin{aligned} S_{\rm bath} &= \sum_\alpha\sum_n\int_0^\Omega d\omega b_{\alpha,n}^\dagger(\omega)(\omega+n\Omega-\mathcal{E}_\alpha^{\rm bath})b_{\alpha,n}(\omega) \\ &\equiv \sum_\alpha\sum_n\int_0^\Omega d\omega b_{\alpha,n}^\dagger(\omega)\Big(g_{\rm bath}^{-1}\Big)_n^\alpha(\omega)b_{\alpha,n}(\omega), \end{aligned} \tag{A25}$$

where we define the inverse bare Green's function for the bath as

$$\Big(g_{\rm bath}^{-1}\Big)_n^\alpha(\omega) = \omega + n\Omega - \mathcal{E}_\alpha^{\rm bath}. \tag{A26}$$

Here, $g_{\rm bath}^{-1}$ acts as the inverse operator of the bare bath Green's function $g_{\rm bath}$, satisfying the relation:

$$\Big(g_{\rm bath}^{-1}\Big)_n^\alpha(\omega)g_{{\rm bath},m}^\beta(\omega') = \delta_{\alpha\beta}\delta_{nm}\delta(\omega-\omega'). \tag{A27}$$

The other inverse Green's functions, $G^{-1}, G_{\rm bath}^{-1}$, and g^{-1}, are defined in a similar manner.

3. Effective Action

By completing the square and integrating out the bath fields $b^\dagger$ and b, we obtain the effective interaction action:

$$S_{\rm int} \equiv -\sum_n\sum_{\alpha,\beta,\gamma}\int_0^\Omega d\omega a_{\gamma,n}^\dagger(\omega)|\mathcal{T}_\alpha|^2 g_{{\rm bath},n}^\alpha(\omega)a_{\beta,n}(\omega). \tag{A28}$$

Therefore, the total effective action of the system becomes

$$S + S_{\rm int} = \sum_n\sum_{\alpha,\beta,\gamma}\int_0^\Omega d\omega a_{\gamma,n}^\dagger(\delta_{\beta,\gamma}g_n^{-1}(\omega) - |\mathcal{T}_\alpha|^2 g_{{\rm bath},n}^\alpha(\omega))a_{\beta,n}. \tag{A29}$$

From this expression, we identify the self-energy induced by the bath as

$$\Sigma_n(\omega) = \sum_\alpha |\mathcal{T}_\alpha|^2 g^\alpha_{\mathrm{bath},n}(\omega) = \sum_\alpha \frac{|\mathcal{T}_\alpha|^2}{\omega + n\Omega - \mathcal{E}^{\mathrm{bath}}_\alpha}. \tag{A30}$$

To evaluate the retarded component of the self-energy, which guarantees the causality of the system's response, we must perform an analytic continuation to the upper half of the complex frequency plane. Practically, this is achieved by introducing an infinitesimally small positive imaginary part $i\eta$ ($\eta \to 0^+$) into the denominator of the bare bath Green's function, yielding

$$\Sigma^R_n(\omega) = \sum_\alpha |\mathcal{T}_\alpha|^2 g^{R,\alpha}_{\mathrm{bath},n}(\omega) = \sum_\alpha \frac{|\mathcal{T}_\alpha|^2}{\omega + n\Omega - \mathcal{E}^{\mathrm{bath}}_\alpha + i\eta}. \tag{A31}$$

Using the identity $1/(x+i\eta) = \mathcal{P}\,(1/x) - i\pi\delta(x)$, where $\mathcal{P}$ denotes the Cauchy principal value, the self-energy can be separated into its real and imaginary parts:

$$\Sigma^R_n(\omega) = \mathcal{P}\sum_\alpha \frac{|\mathcal{T}_\alpha|^2}{\omega + n\Omega - \mathcal{E}^{\mathrm{bath}}_\alpha} - i\pi \sum_\alpha |\mathcal{T}_\alpha|^2 \delta(\omega + n\Omega - \mathcal{E}^{\mathrm{bath}}_\alpha). \tag{A32}$$

Here, we introduce the wide-band approximation. This approximation assumes that the density of states of the bath and the coupling strength $|\mathcal{T}_\alpha|^2$ are constant with respect to energy, and that the bandwidth is infinitely wide. Under this approximation, the real part given by the principal value integral can be neglected, as it simply renormalizes the system Hamiltonian by providing a constant shift to the energy. Furthermore, the imaginary part can be regarded as constant with respect to variations in the Floquet energy $n\Omega$ and ω. Thus, we can define an energy-independent relaxation rate Γ as follows:

$$\Gamma \equiv 2\pi \sum_\alpha |\mathcal{T}_\alpha|^2 \delta(\omega - \mathcal{E}^{\mathrm{bath}}_\alpha). \tag{A33}$$

Consequently, in the wide-band limit, the retarded self-energy of the system reduces to an extremely simple form as a purely imaginary constant:

$$\Sigma^R_n(\omega) \approx -i\frac{\Gamma}{2}. \tag{A34}$$

With the retarded self-energy determined, the general lesser Green's function can be evaluated. The z-component of the current density is expressed in terms of this lesser Green's function as

$$J(t) = -i \int \frac{d\boldsymbol{k}}{(2\pi)^3} \int \frac{d\omega}{2\pi} \mathrm{Tr}\left[\tilde{v}^z(\boldsymbol{k}) \boldsymbol{G}^<(\boldsymbol{k},\omega)\right], \tag{A35}$$

where the trace Tr is taken over both the orbital/spin and Floquet indices, and $\boldsymbol{G}^<(\omega)$ is determined by the Dyson equation

$$\boldsymbol{G}^<(\omega) = \boldsymbol{G}^R(\omega)\boldsymbol{\Sigma}^<(\omega)\boldsymbol{G}^A(\omega). \tag{A36}$$

Appendix B: Derivation of the Geometric Representation of the Nonlinear Current

In this Appendix, we rewrite the contributions to the DC current in terms of the geometric quantities of the Bloch bands. Throughout this paper, we use the particle-current convention and omit the overall electric-charge factor.

We first consider the shift current. Using the relation between the interband velocity matrix element and the non-Abelian Berry connection, $v^\alpha_{12} = -i\epsilon_{12}\mathcal{A}^\alpha_{12}$, we evaluate the momentum derivative of the interband velocity matrix element as

$$\begin{aligned}
\partial_a v^b_{12} &= \partial_a \langle u_1|\, \hat{v}^b\, |u_2\rangle \\
&= \langle \partial_a u_1|\, \hat{v}^b\, |u_2\rangle + \langle u_1|\, \partial_a \hat{v}^b\, |u_2\rangle + \langle u_1|\, \hat{v}^b\, |\partial_z u_2\rangle \\
&= -i \sum_{l=1,2} \mathcal{A}^a_{1l} v^b_{l2} + \left(\partial_a \hat{v}^b\right)_{12} + i \sum_{l=1,2} v^b_{1l} \mathcal{A}^a_{l2} \\
&= \left(\partial_a \hat{v}^b\right)_{12} - i(\mathcal{A}^a_{11} - \mathcal{A}^a_{22}) v^b_{12} + i(v^b_{11} - v^b_{22})\mathcal{A}^a_{12}.
\end{aligned} \tag{B1}$$

Rearranging Eq. (B1), we obtain

$$\left(\partial_a \hat{v}^b\right)_{12} = \left[\partial_a + i(\mathcal{A}^a_{11} - \mathcal{A}^a_{22})\right] v^b_{12} + i\mathcal{A}^a_{12}(v^b_{22} - v^b_{11}). \tag{B2}$$

Substituting Eq. (B2) into the numerator of $\bar{J}^{a;bc}_{\rm shift}$ gives

$$\begin{aligned}
\tilde{v}^a_b h_c - \tilde{v}^a_c h_b &= \mathrm{Im}\Big[(\tilde{v}^a_b - i\tilde{v}^a_c)(h_b + ih_c)\Big] \\
&= \frac{A_5^2}{2}\mathrm{Im}\Big[\Big((\partial_a \hat{v}^b)_{12} - i(\partial_a \hat{v}^c)_{12}\Big)(v^b_{21} + iv^c_{21})\Big] \\
&= \frac{A_5^2}{2}\mathrm{Im}\Big[\Big(\{\partial_z + i(\mathcal{A}^a_{11} - \mathcal{A}^a_{22})\}(v^b_{12} - iv^c_{12}) - i\mathcal{A}^a_{12}\{(v^b_{11} - v^b_{22}) - i(v^c_{11} - v^c_{22})\}\Big)(v^b_{12} - iv^c_{12})^*\Big] \\
&= \frac{A_5^2}{2}\left|v^b_{12} - iv^c_{12}\right|^2\Big[\partial_a \arg(v^b_{12} - iv^c_{12}) + \mathcal{A}^a_{11} - \mathcal{A}^a_{22}\Big] - \frac{A_5^2}{2}\mathrm{Re}\Big[\mathcal{A}^a_{12}\{(v^b_{11} - v^b_{22}) - i(v^c_{11} - v^c_{22})\}(v^b_{12} - iv^c_{12})^*\Big] \\
&= \frac{A_5^2}{2}\left|v^b_{12} - iv^c_{12}\right|^2 R^{a;bc}_{12} - \frac{A_5^2}{2}\mathrm{Re}\Big[\mathcal{A}^a_{12}\{(v^b_{11} - v^b_{22}) - i(v^c_{11} - v^c_{22})\}(v^b_{12} - iv^c_{12})^*\Big],
\end{aligned} \tag{B3}$$

where the shift vector is defined by

$$R^{a;bc}_{12,\pm} \equiv \partial_a \arg(v^b_{12} \pm iv^c_{12}) + \mathcal{A}^a_{11} - \mathcal{A}^a_{22}. \tag{B4}$$

For the Weyl Hamiltonian considered here, the quantity inside $\mathrm{Re}[\cdots]$ in the second term of Eq. (B3) is purely imaginary. the second term therefore vanishes identically, and the shift-current contribution becomes

$$\bar{J}^{a;bc}_{\rm shift} = \pi A_5^2 \int \frac{d\boldsymbol{k}}{(2\pi)^3}\left|v^b_{12} - iv^c_{12}\right|^2 R^{a;bc}_{12,-} f_{12}\delta\Big(\epsilon_{12} + \Omega\Big). \tag{B5}$$

To evaluate the resonant momentum integral, we introduce cylindrical coordinates, $k_\perp \equiv \sqrt{k_x^2 + k_y^2}$, and define the resonant momentum $\bar{k} \equiv \Omega/(2v)$. The delta function can then be rewritten as

$$\begin{aligned}
\delta\Big(\epsilon_{12} + \Omega\Big) &= \delta\Big(\Omega - 2vk\Big) \\
&= \delta\Big(\Omega - 2v\sqrt{k_\perp^2 + k_z^2}\Big)\Theta\Big(\bar{k}^2 - k_z^2\Big) \\
&= \frac{\bar{k}}{2v\sqrt{\bar{k}^2 - k_z^2}}\delta\Big(k_\perp - \sqrt{\bar{k}^2 - k_z^2}\Big)\Theta\Big(\bar{k}^2 - k_z^2\Big) \\
&= \frac{\bar{k}}{2vk_\perp}\delta\Big(k_\perp - \sqrt{\bar{k}^2 - k_z^2}\Big)\Theta\Big(\bar{k}^2 - k_z^2\Big),
\end{aligned} \tag{B6}$$

where we have used

$$\delta\Big(g(x)\Big) = \sum_i \frac{\delta(x - x_i)}{|g'(x_i)|}, \tag{B7}$$

with x_i denoting the simple roots satisfying $g(x_i) = 0$. In the present case, the relevant root in the domain $k_\perp \geq 0$ is

$$k_\perp = \sqrt{\bar{k}^2 - k_z^2}, \tag{B8}$$

which exists only for $|k_z| \leq \bar{k}$.

For spin precession in the xy plane, Eq. (B6) gives the shift current along the z direction as

$$\begin{aligned}
\bar{J}^{z;xy}_{\rm shift} &= \frac{A_5^2 v^2}{8\pi^2}\int_{-\infty}^{\infty} dk_z \int_0^{\infty} k_\perp dk_\perp \int_0^{2\pi} d\phi\Big(1 + s\frac{k_z}{k}\Big)^2 R^{z;xy}_{12,-} f_{12}\delta\Big(\Omega - 2vk\Big) \\
&= \frac{A_5^2\Omega}{16\pi^2}\int_{-\bar{k}}^{\bar{k}} dk_z \int_0^{2\pi} d\phi\Big(1 + s\frac{k_z}{\bar{k}}\Big)^2 R^{z;xy}_{12,-} f_{12} \\
&= \frac{A_5^2\Omega}{16\pi^2}\int_{-\bar{k}}^{\bar{k}} dk_z \int_0^{2\pi} d\phi\Big(1 + s\frac{k_z}{\bar{k}}\Big)^2\Big[\partial_z(-\phi) + \mathcal{A}^z_{11} - \mathcal{A}^z_{22}\Big] f_{12} \\
&= 0.
\end{aligned} \tag{B9}$$

Thus, the z-directed shift current vanishes for spin precession in the xy plane.

Next, we consider the injection current. The hybridization amplitude can be expressed in terms of the quantum metric and Berry curvature. In the perturbativ limit, the dispersive factor associated with the real part of the Green's function approaches the Cauchy principal value,

$$\frac{h_z}{h_z^2+\Gamma^2/4} \simeq \mathcal{P}\Big(\frac{1}{h_z}\Big). \tag{B10}$$

The numerator can be decomposed in a manner analogous to that used for the shift current:

$$\begin{aligned}
\tilde{v}_b^a h_b + \tilde{v}_c^a h_c &= \mathrm{Re}\Big[(\tilde{v}_b^a a - i\tilde{v}_c^a)(h_b + ih_c)\Big] \\
&= \frac{A_5^2}{2}\mathrm{Re}\Big[\Big(\Big(\partial_a \hat{v}^b\Big)_{12} - i\Big(\partial_a \hat{v}^c\Big)_{12}\Big)(v_{21}^b + iv_{21}^c)\Big] \\
&= \frac{A_5^2}{2}\mathrm{Re}\Big[\Big(\{\partial_a + i(\mathcal{A}_{11}^a - \mathcal{A}_{22}^a)\}(v_{12}^b - iv_{12}^c) - i\mathcal{A}_{12}^a\{(v_{11}^b - v_{22}^b) - i(v_{11}^c - v_{22}^c)\}\Big)(v_{12}^b - iv_{12}^c)^*\Big] \\
&= \frac{A_5^2}{4}\partial_z\left|v_{12}^b - iv_{12}^c\right|^2 + \frac{A_5^2}{2}\mathrm{Im}\Big[\mathcal{A}_{12}^a\{(v_{11}^b - v_{22}^b) - i(v_{11}^c - v_{22}^c)\}(v_{12}^b - iv_{12}^c)^*\Big].
\end{aligned} \tag{B11}$$

Using the explicit Weyl spinors, the two terms cancel exactly. For example, in the case of $(a,b,c) = (x,y,z)$, we can obtain

$$\tilde{v}_x^z h_x + \tilde{v}_y^z h_y = \frac{A_5^2}{2}\Big[\frac{v^2}{k}\sin^2\theta(1+\cos\theta) - \frac{v^2}{k}\sin^2\theta(1+\cos\theta)\Big] = 0. \tag{B12}$$

Using $v_{12}^a = -i\epsilon_{12}\mathcal{A}_{12}^a$, we find

$$\begin{aligned}
h_b^2 + h_c^2 &= (h_b - ih_c)(h_b + ih_c) \\
&= \frac{A_5^2}{2}(v_{12}^b - iv_{12}^c)(v_{21}^b + iv_{21}^c) \\
&= \frac{(\epsilon_{12}A_5)^2}{2}(\mathcal{A}_{12}^b - i\mathcal{A}_{12}^c)(\mathcal{A}_{21}^b + i\mathcal{A}_{21}^c) \\
&= \frac{(\epsilon_{12}A_5)^2}{2}\Big[\mathcal{A}_{12}^b\mathcal{A}_{21}^b + \mathcal{A}_{12}^c\mathcal{A}_{21}^c + i\mathcal{A}_{12}^b\mathcal{A}_{21}^c - i\mathcal{A}_{12}^c\mathcal{A}_{21}^b\Big] \\
&= \frac{(\epsilon_{12}A_5)^2}{2}\Big[\mathcal{G}_{12}^{bb} + \mathcal{G}_{12}^{cc} - 2\mathrm{Im}\Big(\mathcal{A}_{12}^b\mathcal{A}_{21}^c\Big)\Big] \\
&= \frac{(\epsilon_{12}A_5)^2}{2}\Big(\mathcal{G}_{12}^{bb} + \mathcal{G}_{12}^{cc} - \mathcal{F}_{12}^{bc}\Big).
\end{aligned} \tag{B13}$$

The injection current can therefore be written as

$$\bar{J}_{\mathrm{inj}}^{a;bc} = -2\pi\tau(\Omega A_5)^2\int\frac{d\boldsymbol{k}}{(2\pi)^3}(v_{11}^a - v_{22}^a)\Big(\mathcal{G}_{12}^{bb} + \mathcal{G}_{12}^{cc} - \mathcal{F}_{12}^{bc}\Big)f_{12}\delta\Big(\epsilon_{12} + \Omega\Big). \tag{B14}$$

It is useful to decompose the injection current into its linear and circular parts:

$$\bar{J}_{\mathrm{inj,L}}^{a;bc} \equiv -2\pi\tau(\Omega A_5)^2\int\frac{d\boldsymbol{k}}{(2\pi)^3}(v_{11}^a - v_{22}^a)\Big(\mathcal{G}_{12}^{bb} + \mathcal{G}_{12}^{cc}\Big)f_{12}\delta\Big(\epsilon_{12} + \Omega\Big), \tag{B15}$$

$$\bar{J}_{\mathrm{inj,C}}^{a;bc} \equiv 2\pi\tau(\Omega A_5)^2\int\frac{d\boldsymbol{k}}{(2\pi)^3}(v_{11}^a - v_{22}^a)\mathcal{F}_{12}^{bc}f_{12}\delta\Big(\epsilon_{12} + \Omega\Big), \tag{B16}$$

such that

$$\bar{J}_{\mathrm{inj}}^{a;bc} = \bar{J}_{\mathrm{inj,L}}^{a;bc} + \bar{J}_{\mathrm{inj,C}}^{a;bc}. \tag{B17}$$

We consider spin precession in the yz plane and allow for a tilt along the z direction. We use cylindrical coordinates about the z axis,

$$k_x = k_\perp\cos\phi, \qquad k_y = k_\perp\sin\phi, \qquad k = \sqrt{k_\perp^2 + k_z^2},$$

in which the occupation factor f_{12} is independent of ϕ. The scalar tilt term cancels in the velocity difference $v^a_{11} - v^a_{22}$ and does not modify the interband geometric quantities.

For a single Weyl node of chirality s, the circular injection current can remain finite along the x direction. Using $\mathcal{F}^{yz}_{12} = -sk_x/(2k^3)$, we obtain

$$\begin{aligned}
\bar{J}^{x;yz}_{\mathrm{inj,C}} &= 2\pi\tau(\Omega A_5)^2 \int \frac{d\boldsymbol{k}}{(2\pi)^3}\Big(v^x_{11} - v^x_{22}\Big)\mathcal{F}^{yz}_{12} f_{12}\delta\Big(\epsilon_{12} + \Omega\Big) \\
&= 2\pi\tau(\Omega A_5)^2 \int_{-\infty}^{\infty} dk_z \int_0^{\infty} k_\perp dk_\perp \int_0^{2\pi} \frac{d\phi}{(2\pi)^3}\Big(-2v\frac{k_\perp\cos\phi}{k}\Big)\Big(-s\frac{k_\perp\cos\phi}{2k^3}\Big) f_{12}\delta\Big(\Omega - 2vk\Big) \\
&= s\tau\frac{(\Omega A_5)^2 v}{4\pi}\int_{-\infty}^{\infty} dk_z \int_0^{\infty} k_\perp dk_\perp \frac{k_\perp^2}{k^4} f_{12}\delta\Big(\Omega - 2vk\Big) \\
&= s\tau\frac{(\Omega A_5)^2 v}{4\pi}\int_{-\bar{k}}^{\bar{k}} dk_z \int_0^{\infty} k_\perp dk_\perp \frac{k_\perp^2}{\bar{k}^4} f_{12}\frac{\bar{k}}{2vk_\perp}\delta\Big(k_\perp - \sqrt{\bar{k}^2 - k_z^2}\Big) \\
&= s\tau\frac{\Omega^2 A_5^2}{8\pi}\int_{-\bar{k}}^{\bar{k}} \frac{dk_z}{\bar{k}}\left[1 - \Big(\frac{k_z}{\bar{k}}\Big)^2\right] f_{12}|_{k=\bar{k}}\,.
\end{aligned} \tag{B18}$$

Here, $\bar{k} = \Omega/(2v)$, and we have used $\int_0^{2\pi} d\phi\,\cos^2\phi = \pi$. The y and z components vanish upon azimuthal integration, since their integrands are proportional to k_xk_y and k_xk_z, respectively.

Similarly, the linear injection current can remain finite along the z direction. Using

$$\mathcal{G}^{yy}_{12} + \mathcal{G}^{zz}_{12} = \frac{1}{4k^2}\Big(1 + \frac{k_x^2}{k^2}\Big),$$

we obtain

$$\begin{aligned}
\bar{J}^{z;yz}_{\mathrm{inj,L}} &= -2\pi\tau(\Omega A_5)^2 \int \frac{d\boldsymbol{k}}{(2\pi)^3}\Big(v^z_{11} - v^z_{22}\Big)\Big(\mathcal{G}^{yy}_{12} + \mathcal{G}^{zz}_{12}\Big) f_{12}\delta\Big(\epsilon_{12} + \Omega\Big) \\
&= -2\pi\tau(\Omega A_5)^2 \int_{-\infty}^{\infty} dk_z \int_0^{\infty} k_\perp dk_\perp \int_0^{2\pi} \frac{d\phi}{(2\pi)^3}\Big(-2v\frac{k_z}{k}\Big)\frac{1}{4k^2}\Big(1 + \frac{k_\perp^2\cos^2\phi}{k^2}\Big) f_{12}\delta\Big(\Omega - 2vk\Big) \\
&= \tau\frac{(\Omega A_5)^2 v}{8\pi}\int_{-\infty}^{\infty} dk_z \int_0^{\infty} k_\perp dk_\perp \frac{k_z}{k^3}\Big(3 - \frac{k_z^2}{k^2}\Big) f_{12}\delta\Big(\Omega - 2vk\Big) \\
&= \tau\frac{(\Omega A_5)^2 v}{8\pi}\int_{-\bar{k}}^{\bar{k}} dk_z \int_0^{\infty} k_\perp dk_\perp \frac{k_z}{\bar{k}^3}\Big(3 - \frac{k_z^2}{\bar{k}^2}\Big) f_{12}\frac{\bar{k}}{2vk_\perp}\delta\Big(k_\perp - \sqrt{\bar{k}^2 - k_z^2}\Big) \\
&= \tau\frac{\Omega^2 A_5^2}{16\pi}\int_{-\bar{k}}^{\bar{k}} \frac{dk_z}{\bar{k}}\frac{k_z}{\bar{k}}\left[3 - \Big(\frac{k_z}{\bar{k}}\Big)^2\right] f_{12}|_{k=\bar{k}}\,.
\end{aligned} \tag{B19}$$

The x and y components vanish upon azimuthal integration. A finite z component requires an occupation factor that is asymmetric under $k_z \to -k_z$, as can arise from the tilt.

1. Tilted Weyl semimetal

We next consider the z-tilted Weyl Hamiltonian with spin precession in the yz plane. We work at zero temperature and assume $\Omega > 0$, $\Delta > 0$, $0 < u < v$, and $-\Delta/2 \le \mu \le \Delta/2$. The potentially nonzero components are the shift current along y, the circular injection current along x, and the linear injection current along z.

The tilt changes the band energies according to $\epsilon_{n,s} \to \epsilon_{n,s} - suk_z$ but leaves the eigenstates unchanged. Its contribution to the intraband velocity is the same in both bands and therefore cancels in their difference:

$$v^a_{11,s} - v^a_{22,s} = -2v\frac{k_a}{k}. \tag{B20}$$

The interband energy difference also remains unchanged, $\epsilon_{12,s} = -2vk$.

For a Weyl node with chirality s, we write the occupation factor on the resonant surface as

$$f_{12} = \Theta\Big(\frac{\Omega}{2} - \Big|\mu + s\frac{\Delta}{2} + suk_z\Big|\Big). \tag{B21}$$

The node-resolved shift current is then

$$\begin{aligned}
\bar{J}^{y;yz}_{\mathrm{shift,s}} &= \pi A_5^2 \int \frac{d\boldsymbol{k}}{(2\pi)^3} \left| v^y_{12,s} - i v^z_{12,s} \right|^2 R^{y;yz}_{12,-} f_{12} \delta\Big(\Omega - 2vk\Big) \\
&= \pi A_5^2 \int_{-\infty}^{\infty} dk_z \int_0^{\infty} k_\perp dk_\perp \int_0^{2\pi} \frac{d\phi}{(2\pi)^3} \frac{v^2 \cos\theta}{k} \Big(1 + s \sin\theta \cos\phi\Big) f_{12} \delta\Big(\Omega - 2vk\Big) \\
&= \frac{A_5^2 v}{8\pi} \int_{-\bar{k}}^{\bar{k}} dk_z \frac{k_z}{\bar{k}} f_{12} \\
&= \frac{\Omega A_5^2}{16\pi} \int_{-\bar{k}}^{\bar{k}} \frac{dk_z}{\bar{k}} \frac{k_z}{\bar{k}} \Theta\Big(\frac{\Omega}{2} - \Big|\mu + s\frac{\Delta}{2} + suk_z\Big|\Big).
\end{aligned} \tag{B22}$$

For the circular injection current, the relevant Berry-curvature component is

$$\mathcal{F}^{yz}_{12,s} = -s \frac{k_x}{2k^3}. \tag{B23}$$

Using the cylindrical-coordinate expression derived above, we obtain

$$\begin{aligned}
\bar{J}^{x;yz}_{\mathrm{inj,C,s}} &= 2\pi\tau(\Omega A_5)^2 \int \frac{d\boldsymbol{k}}{(2\pi)^3} (v^x_{11,s} - v^x_{22,s}) \mathcal{F}^{yz}_{12,s} f_{12} \delta\Big(\Omega - 2vk\Big) \\
&= s\tau \frac{(\Omega A_5)^2 v}{4\pi} \int_{-\infty}^{\infty} dk_z \int_0^{\infty} k_\perp dk_\perp \frac{k_\perp^2}{k^4} f_{12} \delta\Big(\Omega - 2vk\Big) \\
&= s\tau \frac{\Omega^2 A_5^2}{8\pi} \int_{-\bar{k}}^{\bar{k}} \frac{dk_z}{\bar{k}} \left[1 - \Big(\frac{k_z}{\bar{k}}\Big)^2\right] \Theta\Big(\frac{\Omega}{2} - \Big|\mu + s\frac{\Delta}{2} + suk_z\Big|\Big) \\
&= s\tau \frac{\Omega^2 A_5^2}{8\pi} \int_{-\bar{k}}^{\min\{\bar{k}, K_s\}} \frac{dk_z}{\bar{k}} \left[1 - \Big(\frac{k_z}{\bar{k}}\Big)^2\right].
\end{aligned} \tag{B24}$$

For the linear injection current induced by precession in the yz plane, the relevant quantum-metric combination is $\mathcal{G}^{yy}_{12,s} + \mathcal{G}^{zz}_{12,s}$. For the two Weyl nodes, we have

$$\mathcal{G}^{yy}_{12,+} + \mathcal{G}^{zz}_{12,+} = \frac{1}{4k^2}\Big(1 + \frac{k_x^2}{k^2}\Big), \quad \mathcal{G}^{yy}_{12,-} + \mathcal{G}^{zz}_{12,-} = \frac{1}{4k^2}\Big(1 + \frac{k_x^2}{k^2}\Big). \tag{B25}$$

The node-resolved linear injection current along z is therefore

$$\begin{aligned}
\bar{J}^{z;yz}_{\mathrm{inj,L,s}} &= -2\pi\tau(\Omega A_5)^2 \int \frac{d\boldsymbol{k}}{(2\pi)^3} (v^z_{11,s} - v^z_{22,s}) \Big(\mathcal{G}^{yy}_{12,s} + \mathcal{G}^{zz}_{12,s}\Big) f_{12} \delta\Big(\Omega - 2vk\Big) \\
&= -2\pi\tau(\Omega A_5)^2 \int_{-\infty}^{\infty} dk_z \int_0^{\infty} k_\perp dk_\perp \int_0^{2\pi} \frac{d\phi}{(2\pi)^3} \Big(-2v\frac{k_z}{k}\Big) \frac{1}{4k^2} \Big(1 + \frac{k_\perp^2 \cos^2\phi}{k^2}\Big) f_{12} \delta\Big(\Omega - 2vk\Big) \\
&= \tau \frac{(\Omega A_5)^2 v}{8\pi} \int_{-\infty}^{\infty} dk_z \int_0^{\infty} k_\perp dk_\perp \frac{k_z}{k^3} \Big(3 - \frac{k_z^2}{k^2}\Big) f_{12} \delta\Big(\Omega - 2vk\Big) \\
&= \tau \frac{\Omega^2 A_5^2}{16\pi} \int_{-\bar{k}}^{\bar{k}} \frac{dk_z}{\bar{k}} \frac{k_z}{\bar{k}} \left[3 - \Big(\frac{k_z}{\bar{k}}\Big)^2\right] \Theta\Big(\frac{\Omega}{2} - \Big|\mu + s\frac{\Delta}{2} + suk_z\Big|\Big).
\end{aligned} \tag{B26}$$

Applying the node-dependent integration bounds gives

$$\bar{J}^{z;yz}_{\mathrm{inj,L,+}} = \tau \frac{\Omega^2 A_5^2}{16\pi} \int_{-\bar{k}}^{\min\{\bar{k}, K_+\}} \frac{dk_z}{\bar{k}} \frac{k_z}{\bar{k}} \left[3 - \Big(\frac{k_z}{\bar{k}}\Big)^2\right], \tag{B27}$$

$$\bar{J}^{z;yz}_{\mathrm{inj,L,-}} = \tau \frac{\Omega^2 A_5^2}{16\pi} \int_{-\bar{k}}^{\min\{\bar{k}, K_-\}} \frac{dk_z}{\bar{k}} \frac{k_z}{\bar{k}} \left[3 - \Big(\frac{k_z}{\bar{k}}\Big)^2\right]. \tag{B28}$$

The total current in each channel is obtained by summing the contributions from $s = \pm 1$.